



The microscopic origin of K_0 on granular soils: the role of particle shape

Hao Chen¹ · Shiwei Zhao^{1,2} · Jidong Zhao² · Xiaowen Zhou¹

Received: 21 November 2020 / Accepted: 4 February 2021 / Published online: 24 February 2021
© The Author(s), under exclusive licence to Springer-Verlag GmbH, DE part of Springer Nature 2021

Abstract

The at-rest coefficient of lateral pressure, K_0 , is a critical macroscopic parameter for evaluating stress transmission in granular media for engineering practice. This paper revisits the microscopic origin of K_0 and its corresponding underlying physics based on micromechanics-based theories and numerical simulations, with a focus placed on the effect of particle shape. Two typical kinds of distortion (elongation and blockiness) in particle shape are considered, modeled by ellipsoids and superballs in the discrete element method. One-dimensional compression tests are performed on numerical specimens with dense and loose initial states for different particle shapes. An analytical relationship between K_0 and anisotropy of fabric measures (i.e., contact normal, contact force, and shape-related anisotropy) is established within the stress-force-fabric framework. It is found that the analytical K_0 is consistent with the measured one directly from the simulation regardless of particle shape, verifying a well-established relationship between K_0 and fabric. It is further found that contact force partition of K_0 plays the most prominent role in K_0 compared to contact normal and shape-related partitions. Results also reveal the different influence of shape distortion on K_0 and the corresponding mechanical properties related to K_0 , such as void ratio, mobilized friction angle, and coordination number. More specifically, K_0 has a ‘W’-shape relationship with elongation for dense ellipsoids and an ‘M’-shape relationship with blockiness for superballs.

Keywords Anisotropy · Discrete element method · Earth pressure at rest · Granular soil · Non-spherical

1 Introduction

The at-rest coefficient of lateral earth pressure, K_0 , ($= \sigma_h / \sigma_v$, where σ_h and σ_v are the horizontal and vertical stress, respectively) is a critical macroscopic parameter of granular soils in both theoretical and practical applications, e.g., soil slope design in geotechnical engineering [24]. It remains a challenge to estimate K_0 with a mathematically elegant formula due to complicated behavior of granular media. In practice, the Jaky’s equation [12] has long been commonly employed to predict the K_0 value, given by

$$K_0 = 1 - \sin(\Phi) \quad (1)$$

where Φ denotes the internal friction angle of granular media. Jaky’s equation provides a concise manner to reveal the physical meaning of K_0 by linking it to the internal friction angle.

Simple as it may appear, it is well known that K_0 is influenced by a number of typical factors including void ratio [3, 9, 17, 23], friction angle [12, 28], stress state [25], consolidation state [6, 7, 40, 42], specimen preparation method [8, 26], and particle shape [9, 14, 32, 41]. Particle shape is regarded as one of the most fundamental factors affecting both structure and stress transmission within a granular material. For example, Lirer et al. [16] showed that angular particles with lower breakage stress possess a consistent K_0 value with experimental tests, in good agreement with the Jaky’s equation for loose specimens, whereas the relationship between K_0 and vertical stress is closer to the over-consolidated one for dense specimens with round particles. Lirer et al. [16] presented a further comprehensive experimental study on the effects of

✉ Shiwei Zhao
swzhao@scut.edu.cn

¹ State Key Laboratory of Subtropical Building Science, South China University of Technology, Guangzhou, China

² Department of Civil and Environmental Engineering, Hong Kong University of Science and Technology, Clearwater Bay, Kowloon, Hong Kong

particle shape and particle breakage on the evolution of K_0 in oedometer tests with the focus on particle roundness. Nevertheless, the role of particle shape in K_0 remains unclear due to complex shapes within realistic granular assemblies, e.g., sands. Lee et al. [14] investigated the relationship between K_0 and critical and peak friction angles for different particle shapes, including natural sands, glass beads, and etched glass beads in oedometer tests. It is found that K_0 is significantly related to the critical friction angle for glass beads, but not for angular particles (natural sands) due to the inter-locking effect of angularity. Apart from particle shape, the effect of particle size on K_0 has also been investigated in the literature. For example, researchers found that a specimen with a higher maximum grain size has a lower K_0 value [42].

The aforementioned studies mainly focused on the effect of particle shape on K_0 in experiments. They turned to demonstrate the relation between K_0 and different soil types or particle shape through sophisticated experimental investigations. Indeed, conventional experiments succeed in involving quite a good range of real particles, where K_0 can be, however, interpreted merely from a macroscopic perspective, implying that the roles of microscopic factors (predominantly particle shape) cannot be identified for a better understanding of the underlying physics toward the origin of K_0 . Notably, with the prevailing use of micromechanics-based numerical tools, especially the discrete element method (DEM), in the microscopic investigation of granular materials, it enables to link up and verify the relationship between K_0 and the corresponding fabric by combining numerical and experimental analyses. As reported by [10], the microscopic parameters on fabric (e.g., particle arrangement) should be taken into consideration for exploring the relationship between K_0 and particle shape, in addition to the macroscopic parameter (e.g., internal friction). Further, Guo and Stolle [10] proposed an equation between K_0 and branch vector (a fabric parameter defined as a vector connecting centroids of two particles) and verified its accuracy by a series of experiments. Their results emphasized the distinct effect of branch vector on K_0 and indicated that particle shape can influence K_0 by changing not only internal friction but branch vector and hence the fabric structure. It can be seen that experiment tests assisted by numerical analysis can disclose more information on the origin of K_0 , which emphasizes the importance of numerical tools.

With DEM, the investigation on the relationship between K_0 and fabric parameters has been carried on from a new perspective. For example, Lopera Perez et al. [17] found a linear relationship between K_0 and normal contact force anisotropy quantitatively by carrying out one-dimensional DEM compression, where K_0 increases as normal contact force anisotropy decreases regardless of stress

and strain levels. Furthermore, Gu et al. [7] explored the combined influence of contact normal and contact force anisotropy factors on K_0 with spherical particles in DEM, showing that K_0 is a stronger function of contact force anisotropy than contact normal anisotropy. These previous numerical studies explored the relationship between K_0 and different anisotropy parameters but were limited to using spherical particles. Therefore, it would be of interest to use non-spherical particles in DEM simulations for exploring a more general K_0 -fabric anisotropy relationship with considering particle shape effect. Indeed, de Bono and McDowell [5] conducted a series of DEM simulations with two-ball clumped particles and obtained a positive relation between K_0 and vertical stress, which differs from the previous conclusion [7, 26]. Hence, it remains an open issue to understand the role of particle shape comprehensively in K_0 . There have been few reports on the microscopic investigation of K_0 using non-spherical particles in DEM due to the complexity in contact handling caused by the irregularity in shape.

This work revisits the microscopic origin of K_0 with a focus on particle shape. The open-source discrete element code, *SudoDEM*, is employed to efficiently model non-spherical particles. On modeling non-spherical particles, we herein emphasize two featured distortion of particle shape, i.e., ellipsoids and superballs. These two typical shapes are expected to capture main features of particle shapes in nature, i.e., elongation and asphericity [38]. We explore the relationship between K_0 and macroscopic properties of non-spherical assemblies at the macroscopic scale. A connection is further established between K_0 and microscopic anisotropy factors, such as contact normal and contact force anisotropy.

2 Methodology

2.1 Brief introduction to *SudoDEM*

SudoDEM is an open-source discrete element method code developed by the authors [36, 37], especially for modeling of non-spherical particles, which is hosted at <https://sudodem.github.io>. Interested readers are referred to the literature (e.g., [34–36]) for more details on the theory and background of *SudoDEM*. In this work, non-spherical particles are modeled as two particular super-ellipsoidal particles (ellipsoids and superballs), and a linear-spring contact model in conjunction with the Coulomb friction condition is employed as in the literature [39].

2.2 Super-ellipsoidal particle shape

Super-ellipsoidal particles are widely employed to model complex particle shape [4, 29, 37]. Their corresponding surface function [1] can be defined in a local Cartesian coordinate with five parameters as

$$\left(\left| \frac{x}{r_x} \right|^{\frac{2}{\xi_1}} + \left| \frac{y}{r_y} \right|^{\frac{2}{\xi_1}} \right)^{\frac{\xi_2}{2}} + \left| \frac{z}{r_z} \right|^{\frac{2}{\xi_2}} = 1 \quad (2)$$

where r_x , r_y , and r_z are the semi-major axis lengths along x -, y -, and z - directions, respectively; ξ_1 and ξ_2 are parameters controlling surface blockiness, respectively. For the sake of presentation, two shape descriptors η and ζ are introduced for aspect ratio and blockiness of the particle, respectively, such that $r_z = \eta r_x = \eta r_y$ and $\zeta = \xi_1 = \xi_2$. Aspect ratio and blockiness reflect the change of branch vector and angularity of particles. As two major shape distortions of super-ellipsoidal particles, ellipsoids have a blockiness of 1.0 with varying aspect ratios, while superballs have an aspect ratio of 1.0 with varying blockiness (Fig. 1a). Although the sphericity (Φ) of selected particle shapes has been given, we focus on the two shape descriptors (η and ζ) such that the particle shape distortion can be well quantified, helping clarify the microscopic origin of K_0 .

2.3 Simulation setup

A series of numerical specimens composed of 5000 super-ellipsoidal particles was prepared in the absence of gravity in a cubic container with dimensions of about $1.2 \text{ cm} \times 1.2 \text{ cm} \times 1.2 \text{ cm}$. The particle size distribution is similar to that of Ottawa 20/30 sand (Fig. 1b), in which particle size is the diameter of a sphere with the same volume as the given particle. The values of simulation parameters were selected as follows: particle density (ρ) is $2650 \times 10^6 \text{ kg/m}^3$ (note that a density scaling scheme was adopted to achieve a larger time step as commonly done in the literature, e.g., [39]); friction coefficient between particles (μ) is 0.5; damping ratio (α) is 0.3; walls (boundaries) and particles have identical normal (K_n) and tangential (K_s) stiffness, i.e., $1 \times 10^5 \text{ N/m}$ and $7 \times 10^4 \text{ N/m}$ for K_n and K_s , respectively. Initial void ratios of loose and dense specimens were set to 0.750 and 0.664, respectively. The initial mean stress p_0 was set to 10 kPa at the first stage of isotropic compression (i.e., the so-called consolidation in geomechanics). During the isotropic consolidation, different friction coefficients were selected to yield loose and dense specimens [30, 31]. Then, one-dimensional K_0 compression was performed on the consolidated specimens

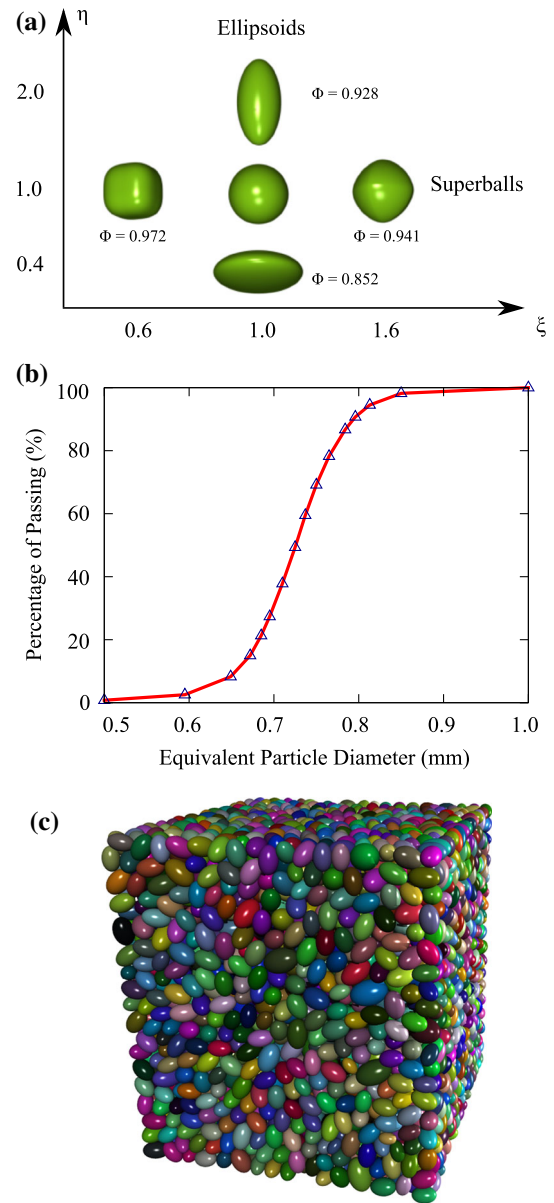


Fig. 1 Schematic diagrams of specimen with **a** particle shapes varying with shape descriptors ζ and η ($\Phi = \pi^{\frac{1}{3}}(6V)^{\frac{2}{3}}/S$ for sphericity, V and S for volume and surface area, respectively); **b** particle size distribution employed in simulation (Ottawa 20/30); **c** an exemplified specimen with ellipsoids (walls are omitted)

to obtain the value of K_0 , where the top and bottom walls moved toward with a suitable constant velocity, while the other sidewalls were maintained stationary. The velocity of moving walls was sufficiently small to ensure a quasi-static loading on the specimen with the dimensionless inertial number (I) given by Eq. (3) below a small value (e.g., 10^{-3} in the literature [20, 36]).

$$I = \dot{\epsilon}_1 \frac{\bar{d}}{\sqrt{\sigma_0/\rho}} \quad (3)$$

where $\dot{\epsilon}_1 = d\epsilon_1/dt$ is the loading strain rate; \bar{d} is the average of particle diameter; σ_0 is the confining stress and ρ is the material density.

2.4 Stress and anisotropy tensors

The homogenized stress within a granular material can be quantified by the well-established Love formula [2], i.e.,

$$\sigma_{ij} = \frac{1}{V} \sum_{c \in V} f_i^c d_j^c \tag{4}$$

where σ_{ij} is the stress tensor; V is volume of the granular material; f_i^c is the i components ($i = 1, 2, 3$) of contact force vector for contact c , and d_j^c is the j components ($j = 1, 2, 3$) of branch vector connecting the centroids of two particles for contact c .

For quasi-static loading, K_0 can be associated with the stress of granular media by

$$K_0 = \frac{p - \frac{q}{3}}{p + \frac{2}{3}q} = 1 - \frac{\frac{q}{p}}{1 + \frac{2q}{3p}} \tag{5}$$

where p and q are the mean and deviatoric stresses, respectively, which can be given by

$$p = \frac{\sigma_{kk}}{3} \tag{6a}$$

$$q = \sqrt{\frac{3}{2} \sigma'_{ij} \sigma'_{ji}} \tag{6b}$$

The analytical relation between stress ratio (q/p) and contact anisotropy, i.e., the stress-force-fabric relationship, has been proposed and verified against simulation data in the previous literature, e.g., for non-spherical particles [19, 38]. Accordingly, it is expected to establish a close form between analytical K_0 and contact anisotropy with the bridge (Eq. (5)) joining K_0 and stress ratio together for non-spherical assemblies. The key derivation is summarized as follows, while the detailed formulas are given in the appendix.

From a perspective of the statistical mechanics of granular materials, the internal stress of granular material can be written in an integration form of contact normal, contact force, and branch vector, given by [19]

$$\sigma_{ij} = \frac{N_c}{V} \int_n E(\mathbf{n}) \bar{f}_i(\mathbf{n}) \bar{d}_j(\mathbf{n}) d\mathbf{n} \tag{7}$$

where σ_{ij} is the stress tensor; N_c is the total contact number; V is the volume of granular material; \mathbf{n} denotes the contact normal vector; $E(\mathbf{n})$ is the probability distribution function (PDF) of contact normal within the granular assembly; $\bar{f}_i(\mathbf{n})$ is the PDF of contact force; $\bar{d}_j(\mathbf{n})$ is the PDF of branch vector. The dyadic product between contact force and branch vector yields tensors involving production between

their components that can be represented by anisotropy tensors in terms of Fourier’s expansion, such as contact normal tensor G_{ij}^e , contact force tensor G_{ij}^f and branch vector tensor G_{ij}^d (see the appendix). Note that both contact force and branch vector tensors have normal and tangential components (i.e., normal contact force tensor G_{ij}^{fn} , tangential contact force tensor G_{ij}^{ft} , normal branch tensor G_{ij}^{dn} , and tangential branch tensor G_{ij}^{dt}). The appendix gives more details on anisotropy tensors.

Taking into account the anisotropy tensors introduced above, Eq. (7) can be rewritten as

$$\begin{aligned} \sigma_{ij} = & \frac{N_c \bar{f}_0 \bar{d}_0}{4\pi V} \int_n (1 + G_{ij}^e n_i n_j) \\ & \times (n_i + G_{ik}^{fn} n_k + (G_{kl}^{fn} - G_{kl}^{ft}) n_k n_i) \\ & \times (n_j + G_{jk}^{dn} n_k + (G_{kl}^{dn} - G_{kl}^{dt}) n_k n_j) d\mathbf{n} \end{aligned} \tag{8}$$

where \bar{f}_0 and \bar{d}_0 are the average normal contact force and the average normal branch vector within the granular assembly, respectively.

Combining Eqs. (5), (6) and (8), K_0 is finally decomposed as:

$$\begin{aligned} K_0 = 1 + & \underbrace{K_0^e + K_0^{fn} + K_0^{ft} + K_0^{ef}}_{\text{contact normal and force partitions}} \\ & + \underbrace{K_0^{dn} + K_0^{dt} + K_0^{ed} + K_0^{fd}}_{\text{shape-related partition}} \end{aligned} \tag{9}$$

where K_0^e denotes the K_0 partition of contact normal; K_0^{fn} and K_0^{ft} are the K_0 partitions of normal and tangential contact force, respectively; K_0^{ef} denotes the combined K_0 partition of contact normal and contact force; K_0^{dn} and K_0^{dt} are the K_0 partitions of normal and tangential branch vector, respectively; K_0^{fd} is combined K_0 partition of normal contact force and branch vector, while K_0^{ed} is that of normal contact force and branch vector. The last four partitions are regarded as shape-related partition. Note that third-order above tensors are neglected in Eq. (9).

To sum up, K_0 can be quantified by contact normal partition, contact force partition, and shape-related partition. The partitions of K_0 in Eq. (9) are similar to that of Gu et al. [7], but a critical difference is that Gu et al. [7] only considered three partitions, i.e., partitions of contact normal, normal contact force and tangential contact force for spherical particles. By contrast, the proposed analytical formula of K_0 has an additional shape-related partition, which can shed light on the role of particle shape in K_0 . It will be verified by DEM results for both ellipsoids and superballs in the following sections.

3 Results and discussion

3.1 Evolution of K_0

The evolution of K_0 with vertical stress (σ_{zz}) of ellipsoids and superballs is presented in Fig. 2 for both dense and loose specimens. The loading processes end at $\sigma_{zz} = 4300$ kPa to prevent excessively particle penetration (e.g., 5% of particle radius). It can be seen that K_0 shows a sharp decrease with the increasing vertical stress first, and then K_0 is expected to approach a stable value with continuous loading. A similar feature was observed in the literature [7, 26]. Note that the final loading stress is selected based on the following consideration. As can be seen, the spheres may reach a stable K_0 at about $\sigma_{zz} = 1300$ kPa similar to that of Lopera Perez et al. [17], but non-spherical particles may need a much higher stress state (even MPa order of magnitude) to reach a stable K_0 , especially in experimental tests [16, 42].

Notably, it is observed that different shape descriptors lead to a variety of stable values of K_0 . Figure 3a, b shows the relationship between stable K_0 and shape descriptors for dense and loose specimens. The variation of stable K_0 with η for dense ellipsoids produces a ‘W’-shape curve; K_0 of ellipsoids has the peak value at $\eta = 0.4$ and a valley one at $\eta = 1.5$. It appears an approximate ‘M’-shape (or inverted ‘V’-shape) relationship between stable K_0 and blockiness for dense superballs. The maximum and minimum of stable K_0 appear at $\xi = 1.2, 1.6$, respectively. It indicates that particle shape can introduce a complicated effect on stable K_0 for dense specimens, which might partially associated with the fabric anisotropy within the specimens. For instance, Zhao et al. [37] reported the variation of random packing density for super-ellipsoidal particles, where the evolution of packing density against the aspect ratio shows an ‘M’-shape, while the relationship between packing density and blockiness presents a ‘V’-shape. Results of Zhao et al. [37] offer an insight to and help explain the variation of K_0 against the shape

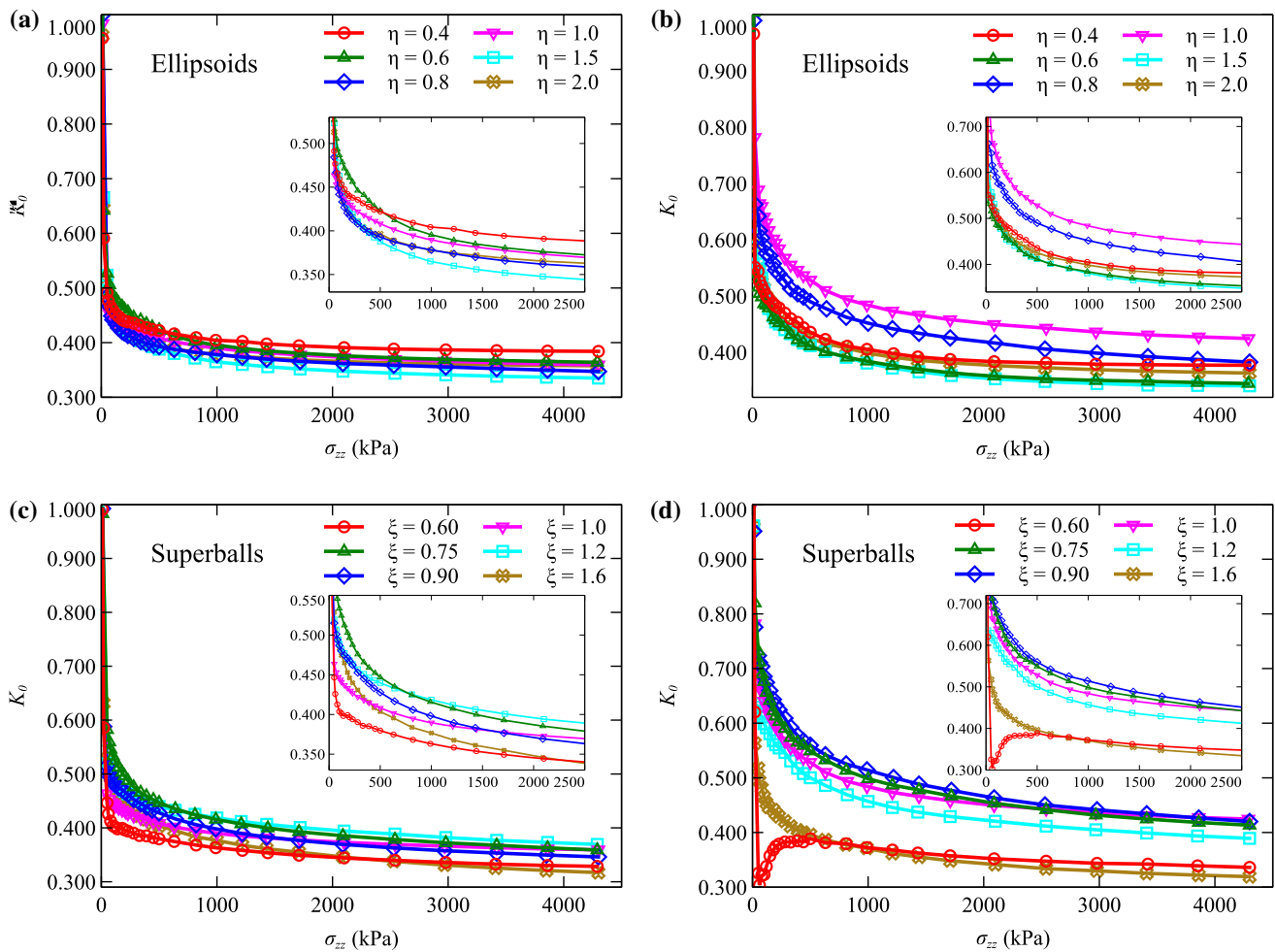


Fig. 2 K_0 of specimen as a function of vertical stress for **a** dense ellipsoids; **b** loose ellipsoids; **c** dense superballs; **d** loose superballs

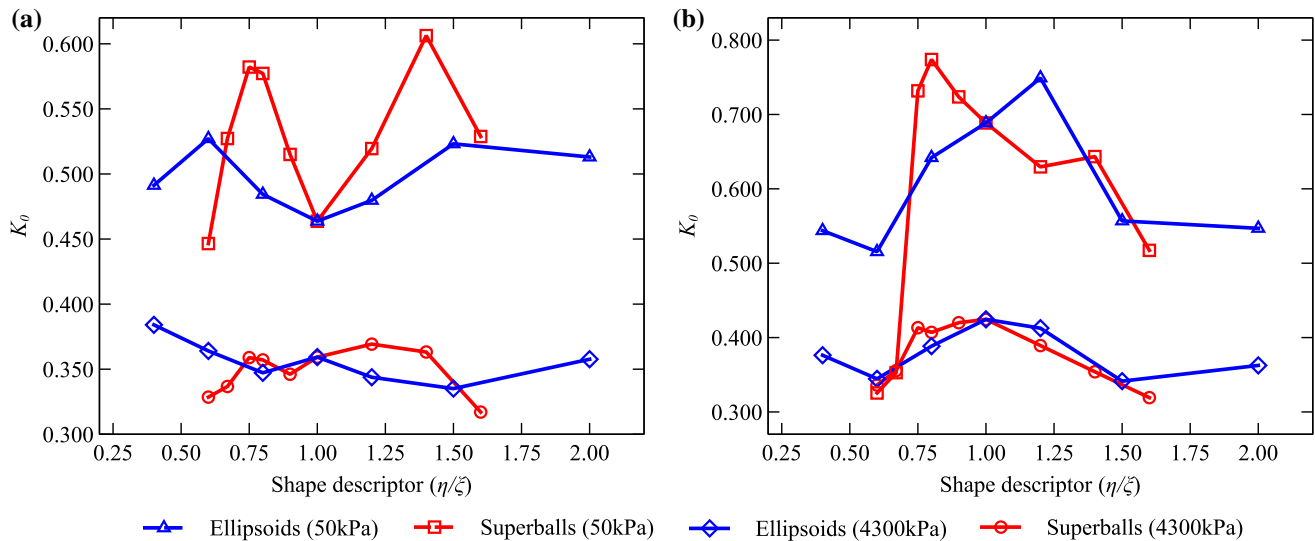


Fig. 3 K_0 versus shape descriptors for **a** dense specimens; **b** loose specimens at $\sigma_{zz} = 50$ kPa and 4300 kPa

descriptors for ellipsoids and superballs. That is, K_0 of the ellipsoids and the superballs are negatively related to their packing density. ‘M’-shape curve of packing density corresponds to the ‘W’-shape curve of K_0 for ellipsoids. In comparison, the shallow ‘M’-shape (inverted ‘V’-shape) K_0 curve of superballs matches the ‘V’-shape curve of packing density. In essence, the packing density of random packing can reflect the resistance of one specimen against the external load. The density of specimens under random packing can be regarded as a characteristic of gravity-induced anisotropy. That is, lower density indicates that gravity has less impact on the evolution of fabric anisotropy. Similarly, for K_0 compression, the vertical external load may be more challenging to play a role in evolving the vertical-dominating anisotropy for specimens with lower packing density. As a result, the force transmission in the vertical direction may be inefficient (higher K_0) due to the indistinct fabric anisotropy. For example, spheres with a minimal packing density as noted by [37] match up with relatively higher K_0 than the other particles (Fig. 3).

However, the particle shape effect on stable K_0 follows a different manner for loose specimens. Figure 3b reveals that K_0 and shape descriptors feature a deeper ‘W’-shape and inverted ‘V’-shape relationship for loose ellipsoids and loose superballs. In particular, K_0 decreases linearly when ζ increases from unity for loose specimens, indicating a more monotonous variation of K_0 for octahedron superballs compared to cubic superballs. That being said, the sphere holds the maximum K_0 among both ellipsoids and superballs. Meanwhile, it can be visually noticed that shape descriptors holding the minimum K_0 in Fig. 3b is almost coincident with that in Fig. 3a. Therefore, it can be concluded that the increase in the initial void ratio partially leads to an increase in the stable K_0 of the sphere,

obviously than the other particles. To sum up, the variation of the stable K_0 against the shape descriptors for whatever dense specimens or loose specimens can be attributed to the similar packing-density-related mechanism as inspired by Zhao et al. [37].

Apart from the stable K_0 , Fig. 3 also presents the initial value of K_0 at $\sigma_{zz} = 50$ kPa for a better understanding of the evolution of K_0 . With vertical stress increasing, strong ‘M’-shape of K_0 versus shape descriptors for dense specimens transforms to shallow ‘W’-shape, and shallow ‘M’-shape (or inverted ‘V’-shape) for ellipsoids and superballs, respectively; simultaneously, deep ‘W’-shape and deep triangle shape for loose specimens become weak ‘W’-shape and soft triangle shape for ellipsoids and superballs, respectively. It illustrates that increasing vertical stress can change both shape and trend of the curve of the relationship between K_0 and shape descriptors, especially for dense specimens. The results emphasize the contribution of the initial void ratio to the evolution of K_0 . In other words, the lower void ratio may cause an inverse variation of K_0 against the shape descriptors compared to the higher void ratio at a lower stress state. One possible reason can be explained as follows: a dense fabric structure may provide a substantial restriction to particle rearrangement, resulting in indistinct induced fabric anisotropy for most of the non-spherical particles. With the dramatic rearrangement of particle orientation or contact normal due to the shape distortion, the induced anisotropic fabric structure may fail to develop. As a result, it would be difficult for most distorted particles to transient their states from initial isotropic to anisotropic except for the cases with highly distorted or spherical particles. From the perspective of stability, highly distorted particles can be significantly unstable after the isotropic consolidation due to remarkable elongation or

angularity, promoting the induced anisotropy. Likewise, the fabric of the spheres can also change easily due to the absence of elongation and angularity during the initial loading stage. Accordingly, highly distorted or spherical particles can possess a more distinct anisotropy than the other particles (lower K_0). That is why it shows an ‘M’-shape curve for the relationship between K_0 and shape descriptors at lower stress. K_0 , regarded as the macro-behavior of fabric anisotropy, is more susceptible to the increase in vertical stress at a lower initial void.

Nevertheless, there is a special case that K_0 of loose superball ($\zeta = 0.6$) keeps nearly unchanged during the loading process. It may be attributed to the cubic-like shape of $\zeta = 0.6$, because the surface-surface contact may dominate the contact network of granular material. The more surface-surface contacts there are, the more stable the granular material is. Even though vertical stress increases continuously, the stress transmission of loose superball ($\zeta = 0.6$) can keep unchanged during the entire loading.

3.2 Particle shape effect on mobilized friction angle and void ratio

The Jaky’s equation predicts K_0 using the internal friction angle from a macroscopic perspective. Nevertheless, it is an open issue to select appropriate internal friction employed in the Jaky’s equation. Indeed, as pointed by Lee et al. [14], it is challenging to set up a unique relationship between K_0 and certain friction angle, such as peak friction angle (Φ_p), critical friction angle (Φ_c), sliding friction angle (Φ_s), and inter-locking friction angle (Φ_g). Accordingly, Lee et al. [14] proposed a relationship between mobilized friction angle (Φ_{mob}) and K_0 directly given as

$$K_0 = \frac{\sigma_{yy}}{\sigma_{zz}} = \frac{1 - \sin \Phi_{mob}}{1 + \sin \Phi_{mob}} \quad (10a)$$

$$\Phi_{mob} = \arcsin \frac{\sigma_{zz} - \sigma_{yy}}{\sigma_{zz} + \sigma_{yy}} \quad (10b)$$

Eq. (10) is expected to help clarify the role of particle shape in K_0 concerning friction angle. As noted by Sadrekarimi et al. [22], particle surface roughness, particle climbing, and particle arrangement can contribute to the mobilized friction angle, which is given as

$$\Phi_{mob} = \Phi_s + \Phi_g \quad (11)$$

where Φ_s denotes the sliding friction angle (note that we take $\Phi_s = \arctan(0.5)$ for all the specimens known as friction coefficient in the material properties for particles (Sect. 2.3)); Φ_g denotes the inter-locking friction angle which implies the particles climbing and arrangement. As the particle surface roughness herein is constant of 0.5, it is necessary to give a more direct comparison between the

actual mobilized friction angle and the intrinsic state variable ($\mu = 0.5$). Because the particle shape adopted here is non-spherical, which means that particle rearrangement or particle climbing is inevitable.

Based on Eq. (11), a normalized mobilized friction angle $\Phi_{mob, norm}$ ($= \Phi_{mob}/\Phi_s$) is introduced to reflect relative magnitude between mobilized friction angle (Φ_{mob}) and sliding friction angle (Φ_s). Relationship between $\Phi_{mob, norm}$ and shape descriptors is shown in Fig. 4. It can be observed a significant uptrend of all the curves of $\Phi_{mob, norm}$ versus shape descriptors as vertical stress increases. Meanwhile, variation of $\Phi_{mob, norm}$ against shape descriptors is contrary to that of K_0 (Fig. 3). For example, there are transformations from initial strong ‘W’-shape to shallow ‘M’- and shallow ‘W’-shape for dense ellipsoids and dense superballs. It is due to the negative relationship between $\Phi_{mob, norm}$ and K_0 as pointed out by Eq. (10a). Moreover, Fig. 4 illustrates that $\Phi_{mob, norm}$ of almost all the dense specimens are larger than unity at the end of loading. The result reflects that the mobilized friction angle exceeds the sliding friction angle. In other words, we can say the inter-locking effect appears for dense specimens herein based on Eq. (11). By contrast, $\Phi_{mob, norm} > \Phi_s$ is observed only for a fraction of loose specimens, especially for those highly distorted loose specimens. The reason may be due to the combined influence of particle regularity and initial void ratio. First of all, the spheres hold an inappreciable inter-locking effect compared to highly distorted shape at a fixed initial void ratio. Besides, as mentioned in Sect. 3.1, granular assembly with a lower initial void ratio is prone to exhibit more intensive interaction between particles than loose specimens. Therefore, loose specimens (especially loose spheres) possess lower inter-locking effects when initial void ratios increase.

Similar to $\Phi_{mob, norm}$, $\Phi_{mob, c}$ is introduced as the proportion of fully mobilized contacts (whose $f_t/f_n = \tan \Phi_s$, where f_t and f_n denote tangential and normal contact force) from a microscopic view. As shown in Fig. 4 (red lines), $\Phi_{mob, c}$ increases weakly as vertical stress increases but can be significantly influenced by particle shape. More specifically, the relationship between $\Phi_{mob, c}$ and shape descriptors produces ‘V’-shape and horizontal line shape for ellipsoids and superballs, respectively. With shape descriptors deviating from unity, $\Phi_{mob, c}$ of ellipsoids increases distinctly, but $\Phi_{mob, c}$ of superballs remains constant. It signifies that $\Phi_{mob, c}$ is more sensitive to aspect ratio than blockiness. Note that Fig. 4 also presents that the trend of $\Phi_{mob, c}$ is not consistent with $\Phi_{mob, norm}$, especially for dense specimens. As noted in Sect. 3.1, the nonlinear relationship between K_0 and shape descriptors results from the restricted particle rearrangement. Likewise, it can be the same reason for the varying relationship between

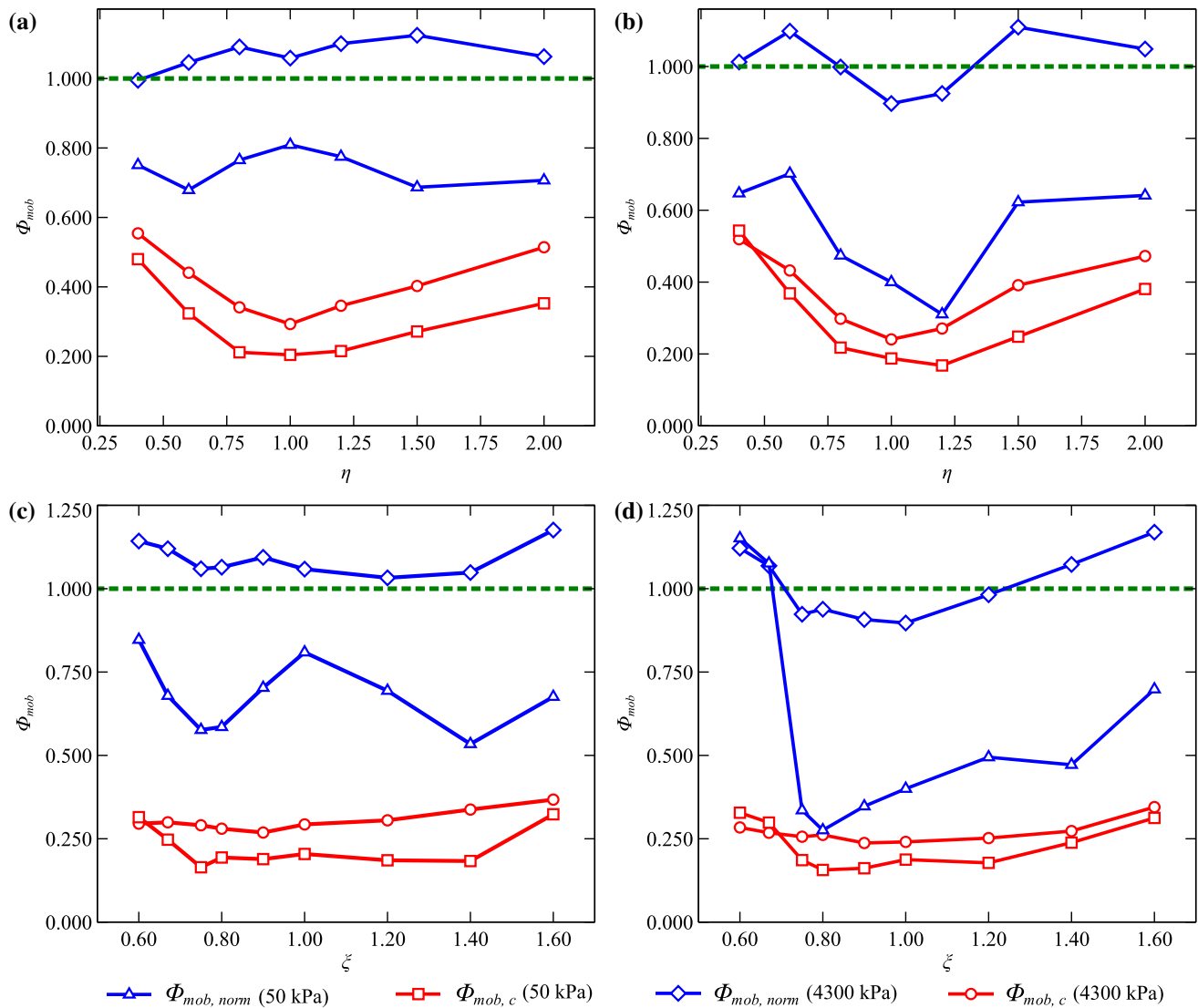


Fig. 4 Curves of $\Phi_{mob, norm}$, $\Phi_{mob, c}$ and shape descriptors for **a** dense ellipsoids; **b** loose ellipsoids; **c** dense superballs; **d** loose superballs

$\Phi_{mob, c}$ and Φ_{mob} . Namely, shape distortion contributes to the different trend of $\Phi_{mob, c}$, i.e., obvious and non-obvious ‘V’-shape of the $\Phi_{mob, c}$ for ellipsoids and superballs, respectively. Then, the actual trend of the mobilized friction angle depends on whether the restricted particle rearrangement exists. Higher void ratio (without restriction) brings on the consistent trend between $\Phi_{mob, c}$ and Φ_{mob} while lower void ratio (with restriction) contributes to the non-consistent trend.

The initial void ratio can be regarded as an essential factor influencing K_0 . Figure 5 shows the evolution of the void ratio against the logarithm of vertical stress for dense and loose specimens, respectively. It can be found that the void ratio of dense samples decreases slowly first, but gradually decreases more sharply with continuous loading. Such a feature is consistent with the previous report [18]. Particularly, Fig. 5a, c reveal that curves of void ratio and

vertical stress move upward when the shape descriptors are close to unity. The difference is that curves of dense ellipsoids are almost overlapped, while curves of dense superballs separate from each other. Given fixed vertical stress, the gap of void ratio for dense superballs is significant, suggesting that the void ratio variation is more affected by blockiness than aspect ratio.

Different from dense specimens, curves of void ratio and vertical stress for loose samples present a sharp decline at initial loading (Fig. 5b, d). It can be explained with an unstable fabric state within loose specimens. Upon the completion of isotropic consolidation, a metastable state can appear due to a higher initial void ratio. As a consequence, the fabric structure of loose specimens may become too fragile to bear the increasing vertical stress and leads to the sharp decline of the void ratio (or so-called swept-out effect [33]). Notably, it is found that loose

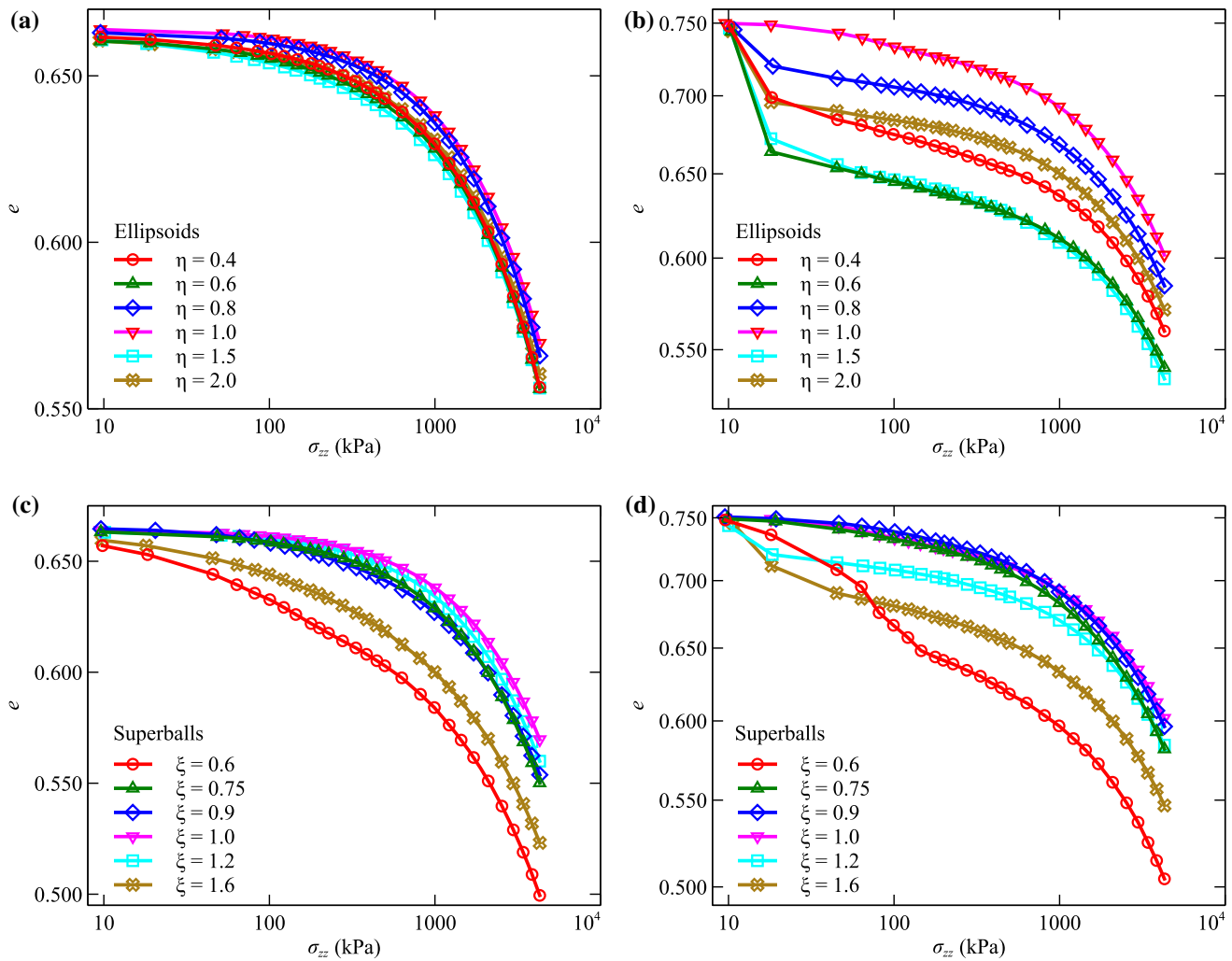


Fig. 5 Variation of void ratio against vertical stress for **a** dense ellipsoids; **b** loose ellipsoids; **c** dense superballs; **d** loose superballs

ellipsoids ($\eta = 0.6, 1.5$) and loose superballs ($\zeta = 0.6, 1.6$) are expected to experience the most significant drop in void ratio. Thus, higher $\Phi_{mob, norm}$ may cause a more dramatic swept-out effect of void ratio for loose specimens. Meanwhile, this result also implies what works on K_0 in the different loading stages. As the vertical stress increases, the specimens may go through two phases: one for the dramatic particle rearrangement, the other for the formation of the force anisotropy. Phase one shows the transition between the isotropic state and the anisotropic state. This phase is accompanied by significant reconfiguration of particle position or orientation but the slight variation of the void ratio variation. The reason can be that the particle reconfiguration is more likely to be isotropic but not anisotropic. On the contrary, phase two demonstrates the significantly evolved force anisotropy, which can promote the force transmission in the vertical direction and results in a more sharp decline of the void ratio. Overall, the clear downtrend of K_0 is relevant to the fabric state transition in

phase one, while the sharp decline of the void ratio is closely associated with the dramatically induced force anisotropy in phase two.

3.3 Evolution of coordination number

The coordination number (CN) is defined as the number of particles in contact with a given particle. The literature has reported a strong correlation between CN and K_0 [7]. Higher CN can help the specimen resist the axial load effectively and result in a smaller K_0 . Therefore, we conduct further examination on the shape effect on the relationship between K_0 and CN (note that mean coordination number overall particles is considered, denoted by MCN).

We first investigate the evolution of MCN against the void ratio (e), aiming to reveal granular fabric development. Figure 6 shows that MCN increases as the void ratio decreases and is expected to reach a relative stable value, especially for spheres. Notably, the MCN can have a more

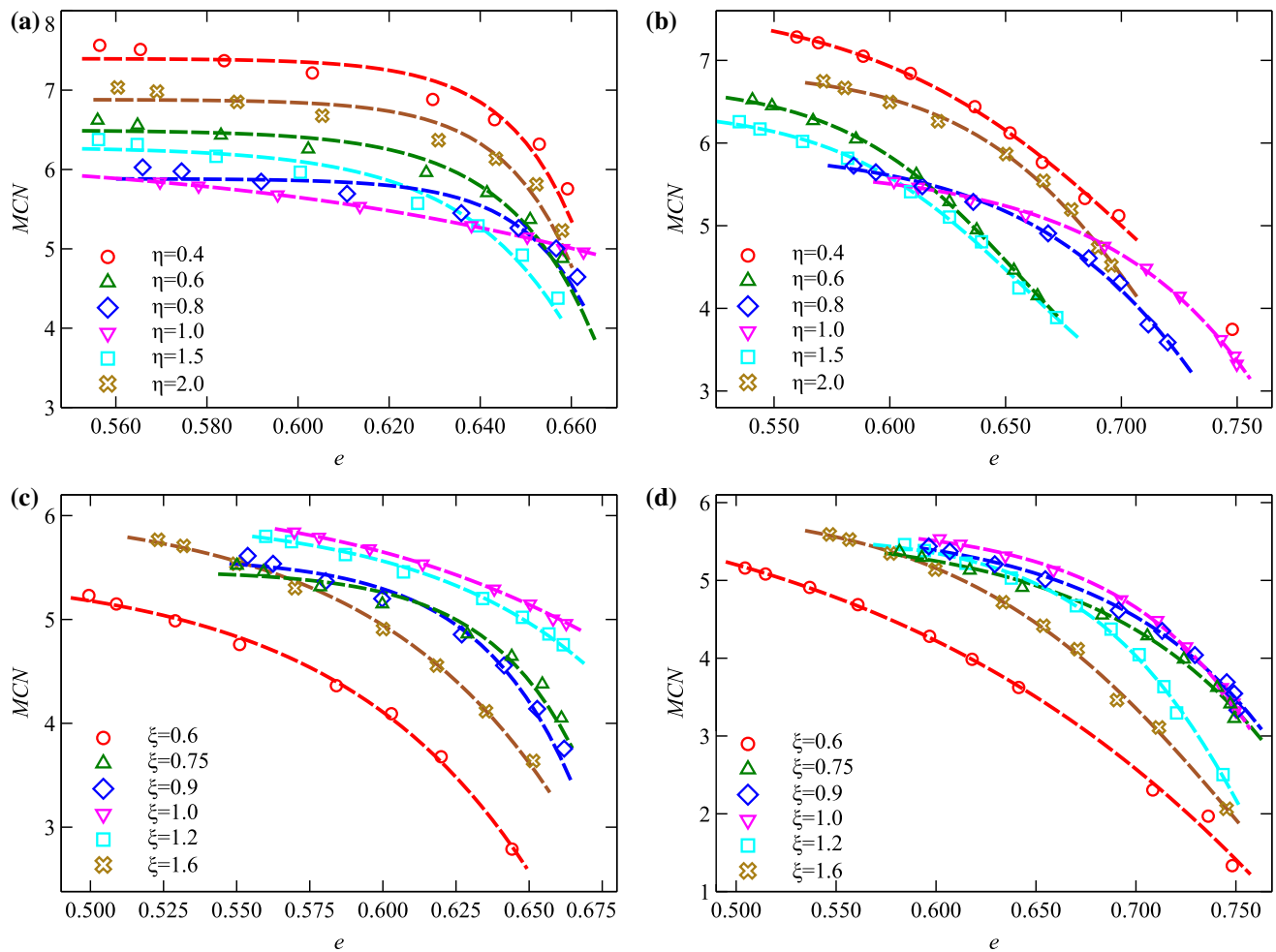


Fig. 6 Relationship between MCN and e for **a** dense ellipsoids; **b** loose ellipsoids; **c** dense superballs; **d** loose superballs

significant uptrend at the lower vertical stress for nearly all the specimens, which corresponds to the sharp decrease in the K_0 . To some extent, the decreasing K_0 at the initial loading stage can be related more closely to the dramatic rearrangement particle position or orientation. As for the final loading stage, the increasing tendency of both MCN and K_0 of most particles can diminish. We call this non-obvious uptrend a quasi-critical state, resulting from the fully developed force anisotropy due to higher stress level. The result reflects that MCN for spheres has reached the quasi-critical state, but MCN of the highly distorted particles still increases monotonically even though the void ratio reaches small enough. It suggests that part of irregular particles can go through a more dramatic fabric structure reconfiguration even at a higher stress level. Thus, it accounts for that K_0 of non-spherical particles may converge at higher vertical stress (Sect. 3.1). In other words, the converge of K_0 is closely correlated with the developed force anisotropy. Moreover, it is also observed that with shape descriptors deviating from unity, MCN - e curves

move upward and downward for ellipsoids and superballs, respectively, implying that the aspect ratio and blockiness exert a contrary effect on the relationship between MCN and e . Elongation of particle shape leads to a higher MCN of prolate/oblate ellipsoids than sphere, while higher angularity of superballs produces lower MCN . Zhao et al. [37] reported an ‘M’-shape relationship between MCN and η for super-ellipsoidal particle assemblies generated by random packing. In particular, Zhao et al. [37] pointed out that the sphere holds a minimum of MCN among ellipsoids and superballs. However, such a feature may disappear during the evolution of MCN under K_0 condition. One highlighted reason is associated with the different levels of stress within the assemblies due to the loading process. With the increase in vertical stress, the granular assembly may undergo a profound change of particle rearrangement. Point-to-point contacts can dominate the entire granular assembly for superballs. Potent contact force as a result of a point-to-point contact type may help to bear the external load. This explains why a granular assembly composed of

superballs does not need higher contact density (i.e., *MCN*). As for ellipsoids with significant distortion ($\eta = 0.4, 2.0$), it is more likely to reconfigure particle orientation, resulting in relatively fragile fabric. As a consequence, ellipsoids need more contacts to resist increasing vertical stress. That is why *MCN* of ellipsoids is higher than superballs.

Figure 7 shows the relationship between *MCN* and K_0 . During the compression, K_0 is expected to decrease as *MCN* increases, which is consistent with the result of Gu et al. [7]. Note that even though increasing vertical stress leads to increased lateral and vertical stress, the vertical stress can grow faster than the lateral one. That is, higher *MCN* corresponds to the lower K_0 . Nevertheless, the relationship between *MCN* and K_0 varies with particle shapes, especially for highly distorted particles. Hence, the curves in Fig. 7 are divided into two groups: Group I with highly distorted particles ($\eta = 0.4, 2.0$ and $\zeta = 0.6, 1.6$), and Group II for other shapes. Curves in Group I exhibit a wide distribution, especially for dense ellipsoids.

Specifically, it is observed that K_0 of ellipsoids in Group I is larger than that in Group II, while K_0 of superballs in Group I is significantly less than that in Group II, if given identical *MCN*. It can be concluded that particles except highly distorted ones possess a similar relationship between K_0 and *MCN*.

Moreover, highly distorted ellipsoids and superballs reveal the different variations of K_0 and e at fixed *MCN*. It may be attributed to the contact of granular assemblies. Deviation of aspect ratio produces prolate (e.g., $\eta = 2.0$) and oblate (e.g., $\eta = 0.4$) shapes, while varying of block-iness results in cube-like (e.g., $\zeta = 0.6$) or octahedron-like (e.g., $\zeta = 1.6$) shapes. Zhao et al. [37] reported that it is more likely for a prolate or oblate ellipsoid to align near the horizontal plane. Furthermore, the corresponding contact distribution may be preferentially non-uniform and have difficulty for particle rearrangement to resist against the axial load. Alternatively, we can say that this contact type is not efficient for stress transmission. Thus, a higher *MCN* is needed for prolate/oblate ellipsoids to bear the external

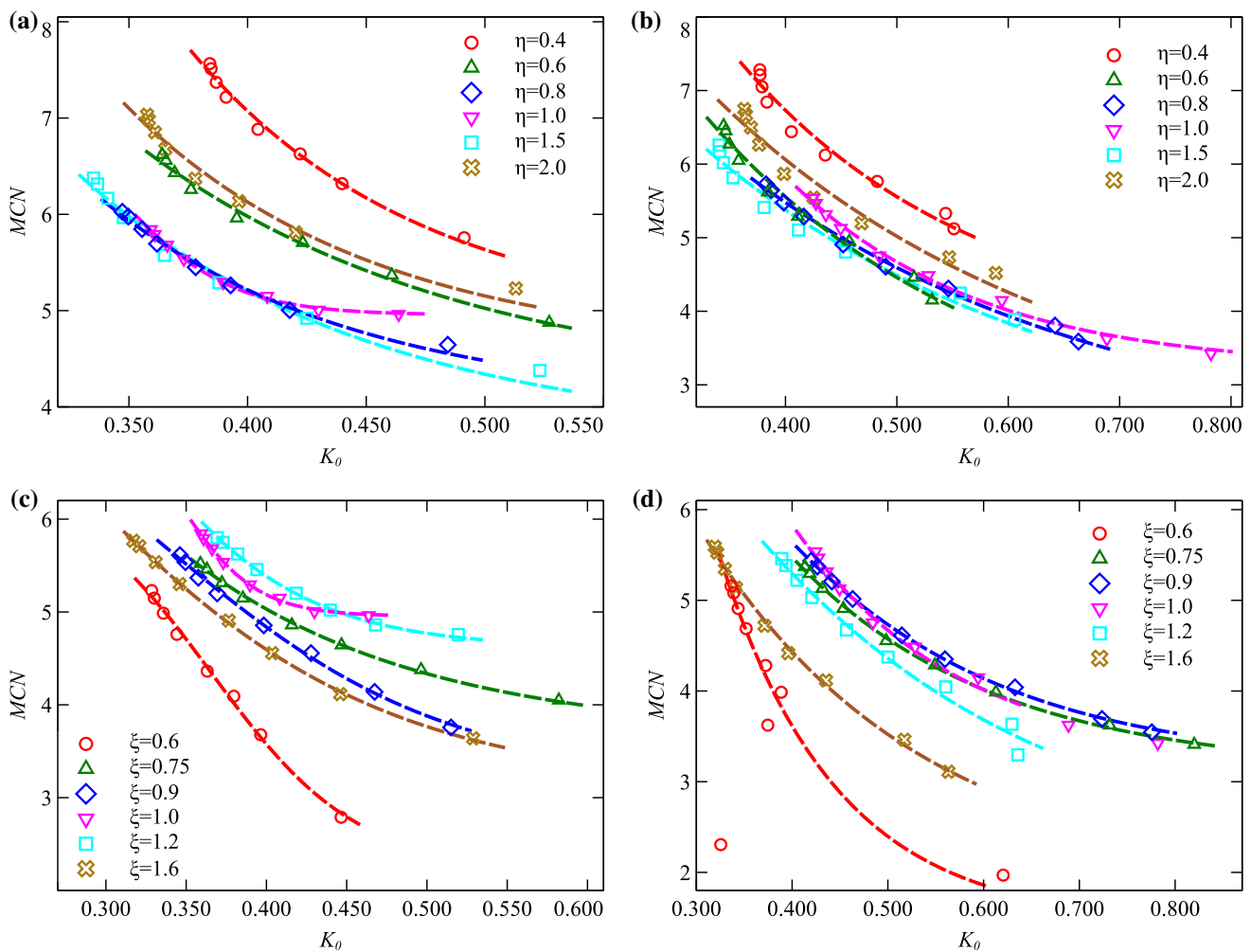


Fig. 7 *MCN* as a function of K_0 for **a** dense ellipsoids; **b** loose ellipsoids; **c** dense superballs; **d** loose superballs

load. Regarding the highly distorted superballs, their shape range is more uniform in three-dimensional space (identical major axis) and can benefit from the dominant point-to-point contact. The particle can easily transmit the force with uniform particle shape and does not need a higher *MCN*.

Notably, Fig. 7a, b shows that a higher initial void ratio can eliminate the shape effect on the relationship between *MCN* and K_0 for ellipsoids. The distance between red and cyan lines becomes narrower as the initial void ratio increases from Fig. 7a to Fig. 7b. By contrast, the difference of *MCN*- K_0 curve between the sphere and highly distorted superballs becomes more significant as the initial void ratio increases. *MCN*- K_0 curves of superballs ($\xi \in (0.75, 1.2)$) are coincident with each other but far away from that of superballs ($\xi = 0.6, 1.6$). We may conclude that the relationship between *MCN* and K_0 is more sensitive to aspect ratio at a lower initial void ratio, but can be affected by blockiness obviously at a higher initial void ratio.

3.4 Relationship between K_0 and anisotropy parameters

The relationship between macroscopic properties and microscopic anisotropy has been attracting increasing attentions [7, 11]. With the stress-fabric-force framework [19, 36], an analytical relationship bridging K_0 and granular anisotropy is introduced in Eq. (12), where the shape-related partition is included in addition to the contact normal and contact force partition.

$$K_0^a = 1 + K_0^e + K_0^{fn} + K_0^{fi} + K_0^{ef} + K_0^s \quad (12a)$$

$$K_0^s = K_0^{ed} + K_0^{fd} + K_0^{dn} + K_0^{di} \quad (12b)$$

where K_0^a is the analytical K_0 derived from granular anisotropy; K_0^s denotes shape-related partition of K_0 , and the other symbols are partitions of K_0 defined in Eq. (9). The contribution of each partition of K_0 will be examined in the following sections.

Figure 8 presents the evolution of measured (red solid line) and analytical (red dash line) K_0 for dense ellipsoids. The analytical K_0 is consistent with the measured one, suggesting that the established analytical solution to K_0 in Eq. (12) can be employed to investigate the origin of K_0 from a microscopic point of view.

On the whole, K_0 exhibits a sharp decrease with σ_{zz} and approaches a nearly constant value as the σ_{zz} continuously increases from about 50 kPa (Fig. 2). The impact of contact anisotropy on K_0 may be disparate for the two loading stages of $\sigma_{zz} < 50$ kPa and $\sigma_{zz} \geq 50$ kPa considering the different decline of K_0 . Furthermore, the variation of each K_0 partition is shown in Figs. 8 and 9 for dense ellipsoids

and dense superballs, respectively. It can be found that the decrease in normal contact force partition (K_0^{fn}) is the most significant one among all the K_0 partitions. Meanwhile, K_0^{fn} plays the most vital part in K_0 for all specimens, specifying that K_0 is mainly influenced by the K_0^{fn} . This result is consistent with that of Gu et al. [7], which revealed that the variation of K_0 chiefly results from the distinction of normal contact force anisotropy. However, this study carries with more findings as that tangential contact force partition (K_0^{fi}) can exert an equivalent effect on K_0 as K_0^{fn} for highly distorted ellipsoids such as $\eta = 0.4, 2.0$ (see Fig. 8a, f). This result reveals the different influence of shape distortion on the K_0 (in detailed, on K_0^{fn} and K_0^{fi}). Deviation of aspect ratio from unity leads to the increasing ratio of K_0^{fn} and K_0^{fi} . Nevertheless, this ratio is hardly affected by the deviation of blockiness as it can be observed that the dominating role of K_0^{fn} in K_0 is independent of the variation of blockiness. For this reason, we focus on not only the influence of single varying shape descriptors (η/ξ) on K_0 partitions but the different impact between the two shape descriptors.

Considering the marked difference in downtrend of K_0 against the vertical stress, we take the state $\sigma_{zz} = 50$ kPa as the initial state and $\sigma_{zz} = 4300$ kPa as the final state for a further investigation of shape effect on K_0 partitions. Figure 10a shows the K_0 against aspect ratio for dense ellipsoids as an ‘M’-shape at the initial state, but ‘W’-shape at the final state. Such a significant contrast on K_0 curve between different loading stages can be attributed to the combined effect of K_0^{fn} and K_0^{fi} on K_0 . With η deviating from unity, the shape distortion caused by aspect ratio brings about the contrary effect as increasing K_0^{fn} and decreasing K_0^{fi} . Since the increase in K_0^{fn} outpaces the decrease in K_0^{fi} , highly distorted ellipsoids can have higher K_0 than spheres at the initial state. Likewise, the deviation of aspect ratio results in a more dramatic decreasing trend of K_0^{fi} but a gentle uptrend for K_0^{fn} , which explains why the minimal K_0 transients from sphere to $\eta = 1.5$ at the final state. It demonstrates that the aspect ratio can have a more remarkable impact on K_0^{fn} at the initial state but K_0^{fi} at the final state. Compared to ellipsoids, superballs display a different mechanism as to how shape descriptors affect K_0 . As shown in Fig. 10c, relationships between contact force partitions (K_0^{fn} , K_0^{fi}) and blockiness show ‘V’-shape and approximate ‘M’-shape, respectively. The deviation of blockiness from unity leads to the upside-down of K_0^{fn} and continuous increase in K_0^{fi} . As the σ_{zz} increasing, relationship between K_0^{fn} or K_0^{fi} and blockiness changes from ‘M’-shape or ‘V’-shape to monotonic one. With blockiness

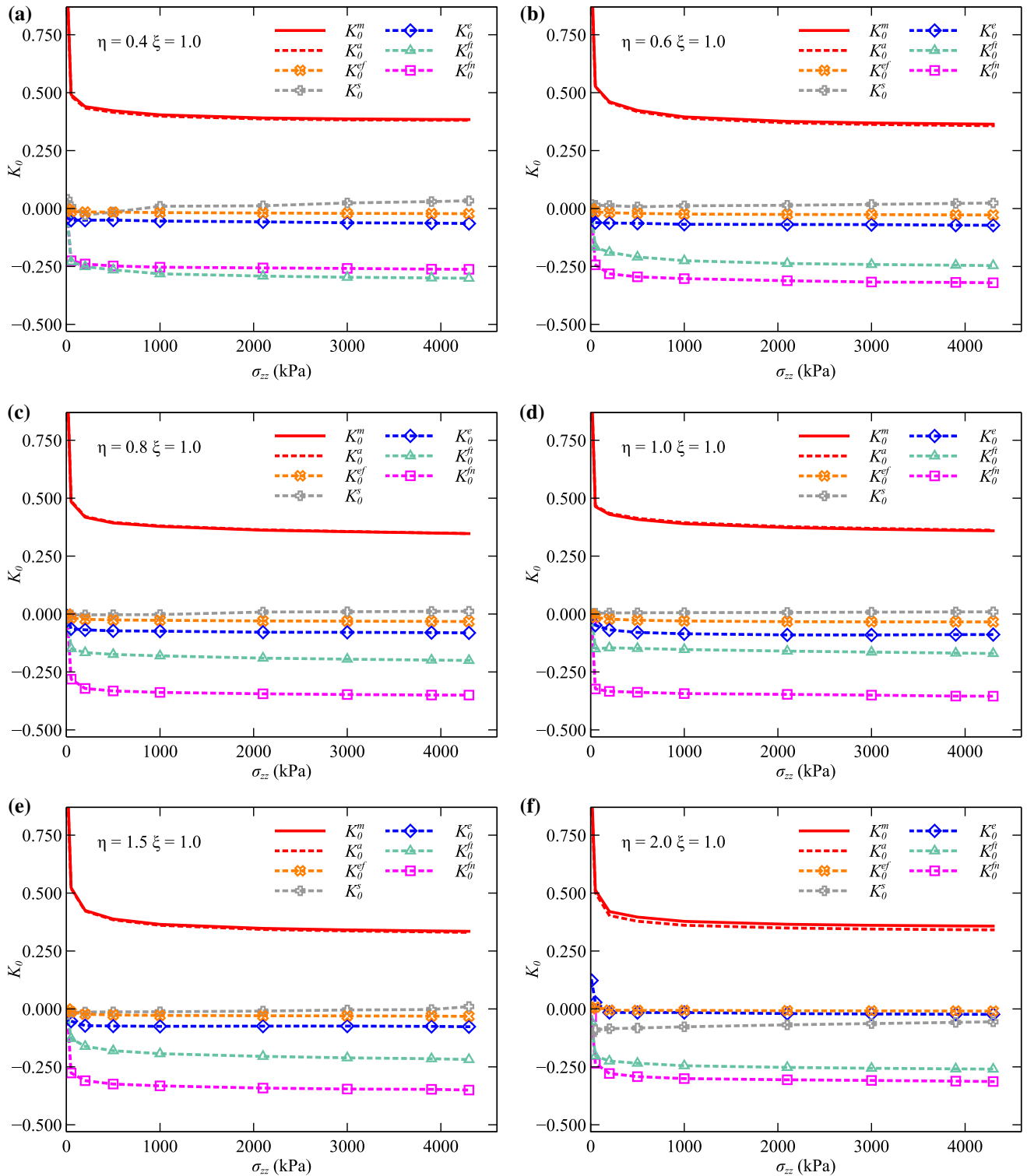


Fig. 8 Variation of K_0 and its partitions for dense ellipsoids

increasing from 0.6 to 1.6, K_0^{fn} and K_0^{fi} present uptrend and downtrend, respectively. Furthermore, it can be found that the blockiness effect on the contact force partition is indistinct compared to the aspect ratio effect. In summary,

Fig. 10 illustrates that stress level changes the sensitive contact force partition of aspect ratio from K_0^{fn} to K_0^{fi} and weakens the effect that blockiness exerts on both K_0^{fn} and K_0^{fi} .

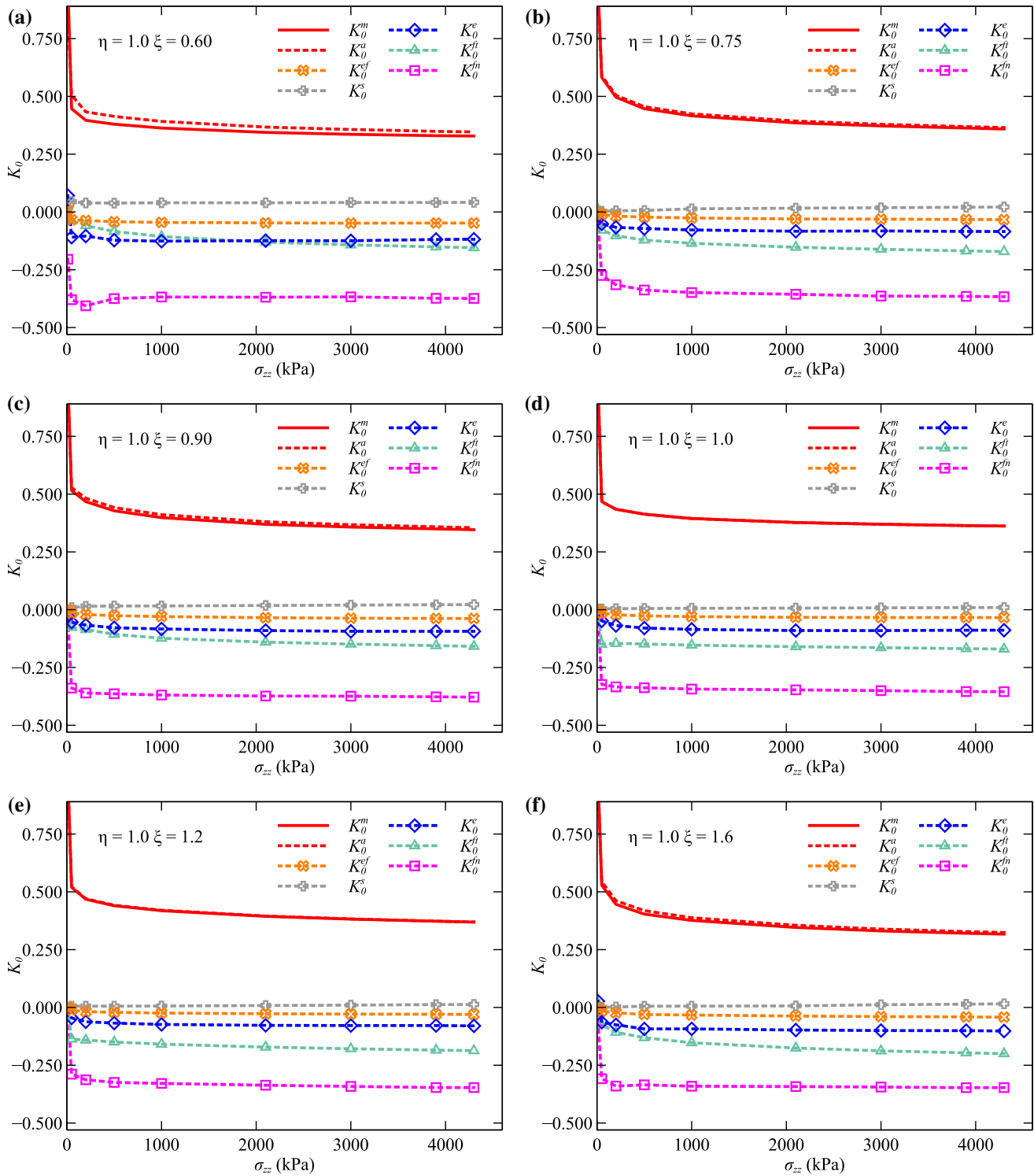


Fig. 9 Variation of K_0 and its partitions for dense superballs

The influence of contact normal and shape-related partitions on K_0 cannot be neglected, even though contact force partitions play an important part in the K_0 as noted. It can be found that both K_0^e and K_0^s can fluctuate greatly for highly distorted ellipsoids ($\eta = 2.0$) and superballs

($\xi = 0.6$) in Fig. 10a, c. However, the fluctuation of K_0^e and K_0^s can diminish as the σ_{zz} increases. One possible reason is that the specimen’s fabric structure can suffer from a dramatic reconfiguration during the initial loading stage. The reconfiguration of fabric structure can be accompanied by a

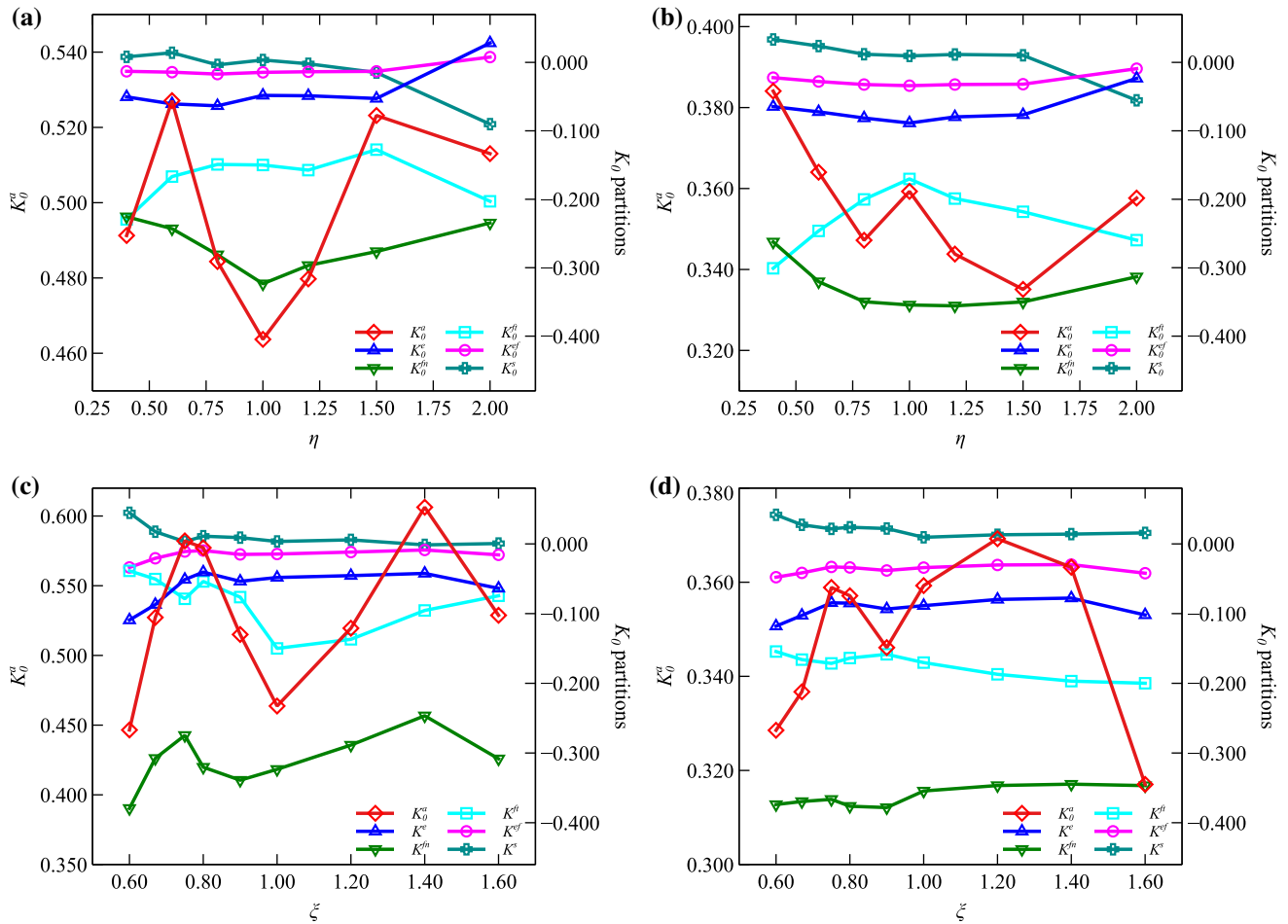


Fig. 10 Shape effect on K_0 partitions for dense specimens **a** initial ellipsoids; **b** final ellipsoids; **c** initial superballs; **d** final superballs

more obvious variation of particle position and orientation. It implies that particle shape can make a difference in the initial loading stage. Nevertheless, the assembly can possess a denser fabric structure at the final state, which may prevent the particle orientation or contact normal. This may explain that the curves of K_0^e and K_0^s at the end of the loading (Fig. 10b, d) are prone to show a smaller range than that at the beginning (Fig. 10a, c). Another point is that aspect ratio and blockiness can exert an opposite impact on K_0^e and K_0^s between highly distorted particles. Deviation of shape descriptor from unity leads to the increasing K_0^e but decreasing K_0^s for ellipsoids, but downtrend of K_0^e and uptrend of K_0^s for superballs. In summary, our results suggest that aspect ratio and blockiness have an inverse impact on the variation of particle shape partitions. Nevertheless, this influence at the final state can be inappreciable compared to that at the initial state.

Figure 11b shows the evolution of K_0 partitions for loose specimens. The shape of K_0 - η/ξ curves holds inverted ‘V’-shape for all the loose specimens. One distinct difference between loose and dense specimens is that curves of K_0 and

shape descriptors of loose specimens can keep their trends from the initial state to the final state. The reason for this can be attributed to the K_0^{fi} . It can be found that increasing σ_{zz} brings up a significant change of the relationship between K_0^{fi} and shape descriptors for dense specimens. For example, the shape effect of ellipsoids on K_0^{fi} can transit from a truncated triangle to an obvious inverted ‘V’-shape as the σ_{zz} increases. The same things go for dense superballs as the influence of blockiness on K_0^{fi} is diminished (from ‘V’-shape to a flatter one) as the σ_{zz} increases. Such a difference between loose and dense specimens reveals that the influence of particle shape on K_0 can differ in tangential contact force anisotropy with the varying void ratios.

This section concludes that K_0 is principally influenced by its contact force partitions. The aspect ratio can have a closer relationship with K_0^n at lower vertical stress and has ties with K_0^f at higher stress level. Nevertheless, increasing vertical stress weakens the blockiness effect on both K_0^{fn} and K_0^{fi} for dense superballs. As for shape-related partitions, aspect ratio and blockiness exert an inverse impact

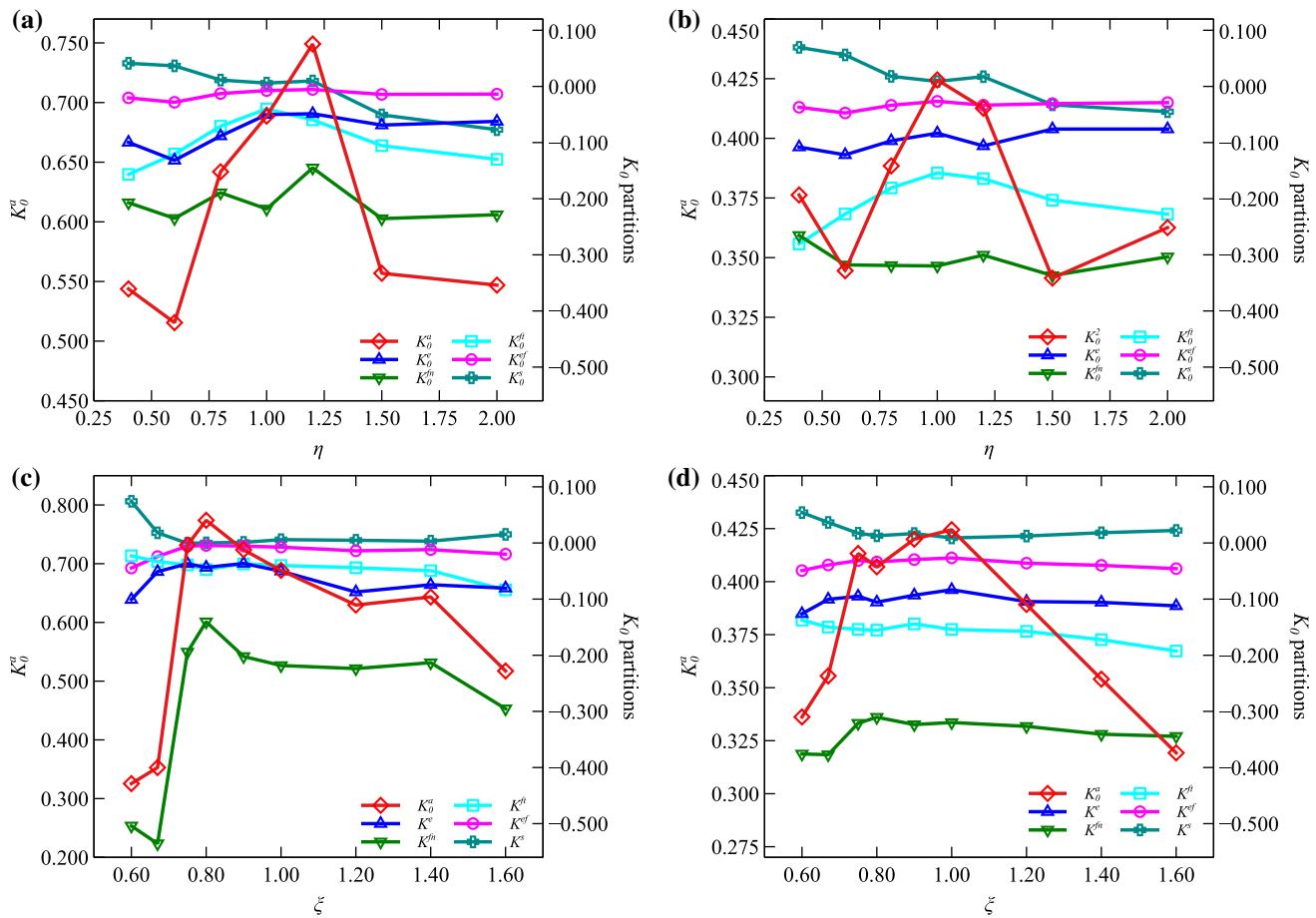


Fig. 11 Shape effect on K_0 partitions for loose specimens **a** initial ellipsoids; **b** final ellipsoids; **c** initial superballs; **d** final superballs

on the shape-related partitions. However, both effects can be weakened as σ_{zz} increases. Furthermore, different particle shape effect on K_0 against the void ratios can be attributed to the stress-independent relationship between K_0^{fn} and shape descriptors that occur only in the loose specimens.

3.5 Influence of contact force on K_0

Lopera Perez et al. [17] investigated the relationship between K_0 and anisotropy quantified by orientations and magnitudes of normal contact force and concluded that the relationship between K_0 and normal contact force anisotropy is independent of stress and strain level. Hence, it is of interest to check whether such a conclusion still holds for non-spherical particles in this section.

Contact force anisotropy (a_n) is defined as $a_n = \sqrt{(3/2)G_{ij}^{fn}G_{ij}^{fn}}$ (where G_{ij}^{fn} denotes the anisotropy tensor of normal contact force). Evolution of a_n against vertical stress is similar to that of K_0 ; that is, they both approach a stable value when vertical stress is large enough (Fig. 12).

Fitting curves depict the particle shape effect on the relationship between a_n and σ_{zz} . When aspect ratio deviates from unity, curves of $a_n \sim \sigma_{zz}$ move downward. Nevertheless, these curves move upward as the deviation of blockiness. It suggests that the sphere has the highest a_n among ellipsoids, but the lowest a_n among superballs. Furthermore, it is observed that curves of $a_n \sim \sigma_{zz}$ for ellipsoids are sparsely distributed, which implies that the relationship between $a_n \sim \sigma_{zz}$ has a stronger relation with aspect ratio than blockiness.

Relationship between stable values of a_n and K_0 is also influenced by particle shape (Fig. 13). Specifically, K_0 is related to a_n linearly and negatively for both ellipsoids and superballs. Nonetheless, the variation of aspect ratio affects the relationship between K_0 and a_n more. As aspect ratio deviates from unity, curves of K_0 and a_n move to the left, while curves for superballs coincide with each other as the deviation of blockiness. It can be put down to the close relationship between aspect ratio and normal contact force component of K_0 (K_0^{fn}). As mentioned in Sect. 3.4, the variation of aspect ratio can lead to a significant change in the K_0 partition of normal contact force.

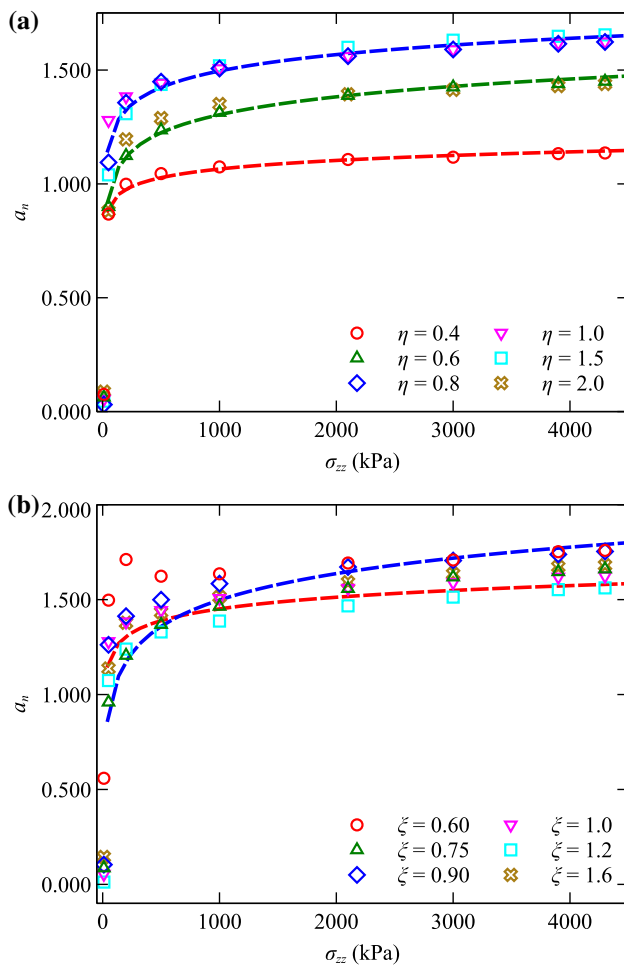


Fig. 12 Anisotropy parameter a_n of normal contact force as a function of vertical stress for **a** ellipsoids; **b** superballs

K_0 reflects the stress transmission of granular assembly in terms of the contact force [6, 27], i.e., K_0 signifies the ratio of horizontal and vertical component of contact force vector in a microscopic view. The contact force angle (θ_k) is introduced to evaluate the contribution of the contact force vector to K_0 .

$$\theta_k = \arctan\left(\frac{f_y}{f_x}\right) \tag{13}$$

where f_x and f_y denote the horizontal and vertical component of the contact force vector. K_0 is negatively related to the θ_k of contacts from the microscopic view. Because an increase in θ_k denotes the increasing difference between f_y and f_x , and K_0 decreases as a result. Radjai et al. [21] reported a bimodal characteristic of stress transmission within a granular material in terms of strong ($F/\bar{F} > 1$) and weak contact force ($F/\bar{F} \leq 1$) where \bar{F} is the average force overall the contact forces in the specimen.

Contours of θ_k of strong and weak contact force are displayed in Fig. 14 for sphere and highly distorted shapes.

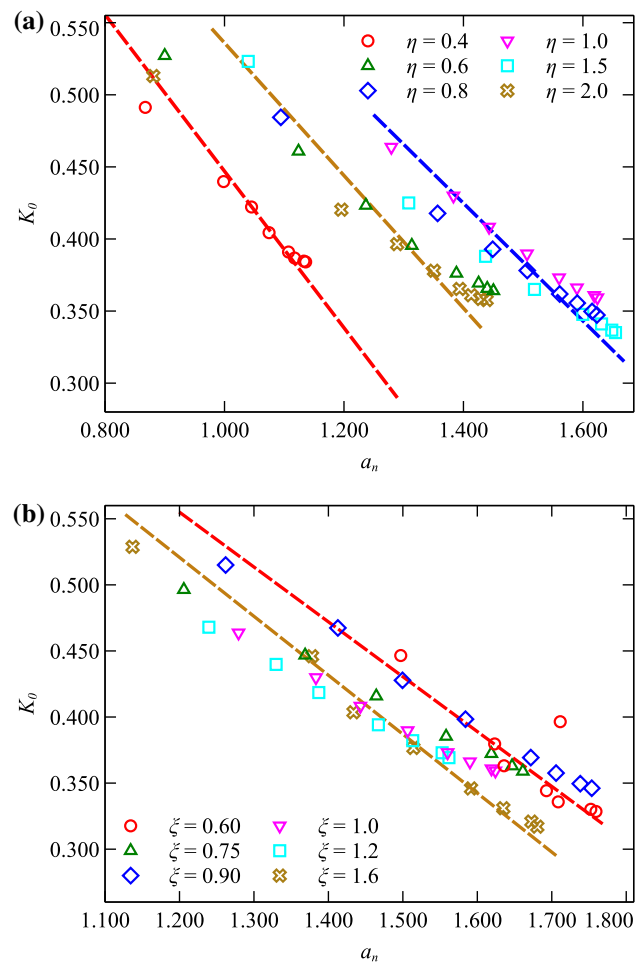


Fig. 13 Relationship between K_0 and a_n for **a** ellipsoids; **b** superballs

Notably, the scope of $\theta \geq 45^\circ$ increases as vertical stress increases for strong contact force but not for weak contact force. It indicates that strong contact force is more sensitive to vertical stress; in other words, a tighter relationship between K_0 and strong contact force appears regardless of particle shape. Due to this, the particle shape effect on the relationship between θ_k of strong contact and K_0 is investigated, and results are shown in Fig. 15 with a binary mixture of the yellow and orange region. The orange area characterizes the contribution of strong contact force to K_0 , which is obtained by *OpenCV* library and normalized by the area of the whole region. Overall, it shows a negative relationship between the area of the orange region and K_0 . That is, strong contact force vector with $\theta_k \geq 45^\circ$ weakens K_0 distinctly. However, special cases exist for $\eta = 0.4$ and $\xi = 0.9$, where both ellipsoids ($\eta = 0.4$) and superballs ($\xi = 0.9$) possess a higher area but higher K_0 than spheres. These special cases may reveal that K_0 is influenced by contact force but not predetermined. The shape-related partition can have a certain impact of K_0 despite the dominating influence of normal contact force on K_0 .

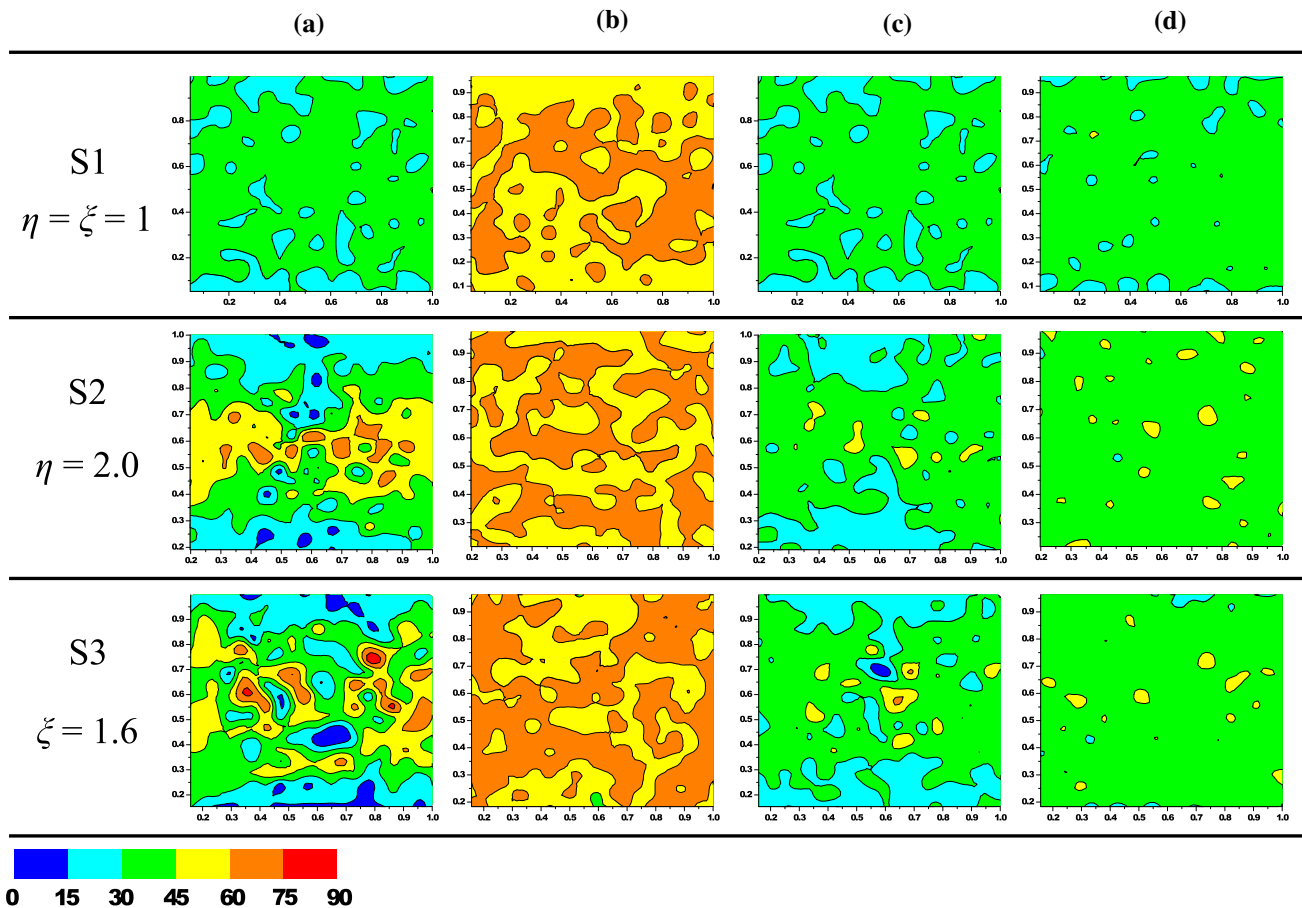


Fig. 14 Evolution of orientation of normal contact force for S1 sphere, S2 ellipsoid and S3 superball at initial state (a, c) and final state (b, d)

4 Conclusion

An analytical relationship between K_0 and anisotropy of microscopic fabric measures is established with the stress-force-fabric framework and is further verified with a series of DEM simulated oedometer tests. The emphasis of the study is placed on the effect of particle shape, where two representative shapes, i.e., ellipsoid and superball, are employed to model particles with different aspect ratios and asphericities, respectively. We examine the effect of particle shape on bridging K_0 and the microscopic fabric measures. Some interesting findings are summarized below.

1. K_0 decreases and approaches a relatively stable value as vertical stress increases. However, stress state can only influence the relationship between K_0 and shape descriptors of dense specimens obviously but not loose specimens. As for the K_0 at the final state specifically, the relationship of stable K_0 -aspect ratio shows a weak 'W'-shape for both dense and loose ellipsoids, and the relationship between stable K_0 and blockiness shows nearly 'M'-form for both dense and loose superballs.
2. Mobilized friction as a key influencing factor of K_0 is investigated in terms of normalized mobilized friction angle ($\Phi_{mob,norm}$) and proportion of fully mobilized contact ($\Phi_{mob,c}$). The variation of $\Phi_{mob,norm}$ reflects that contribution of the inter-locking effect to mobilized friction angle is more evident for dense specimens at the end of the loading stage. Moreover, $\Phi_{mob,c}$ is more likely to be influenced by aspect ratio than blockiness irrespective of the void ratio.
3. Shape descriptors have a more decisive influence on the relationship between e and σ_{zz} for loose specimens than dense specimens. Especially, loose specimens can experience a sharp decrease in void ratio at the beginning of loading due to the swept-out effect of unstable fabric state, which is positively related to the initial mobilized friction angle of the specimen.
4. Highly distorted ellipsoids hold a higher void ratio and higher K_0 than sphere at fixed MCN, which is contrary to highly distorted superballs. In particular, particles except the highly distorted ones possess a similar relationship between MCN and K_0 , more obviously for loose specimens.

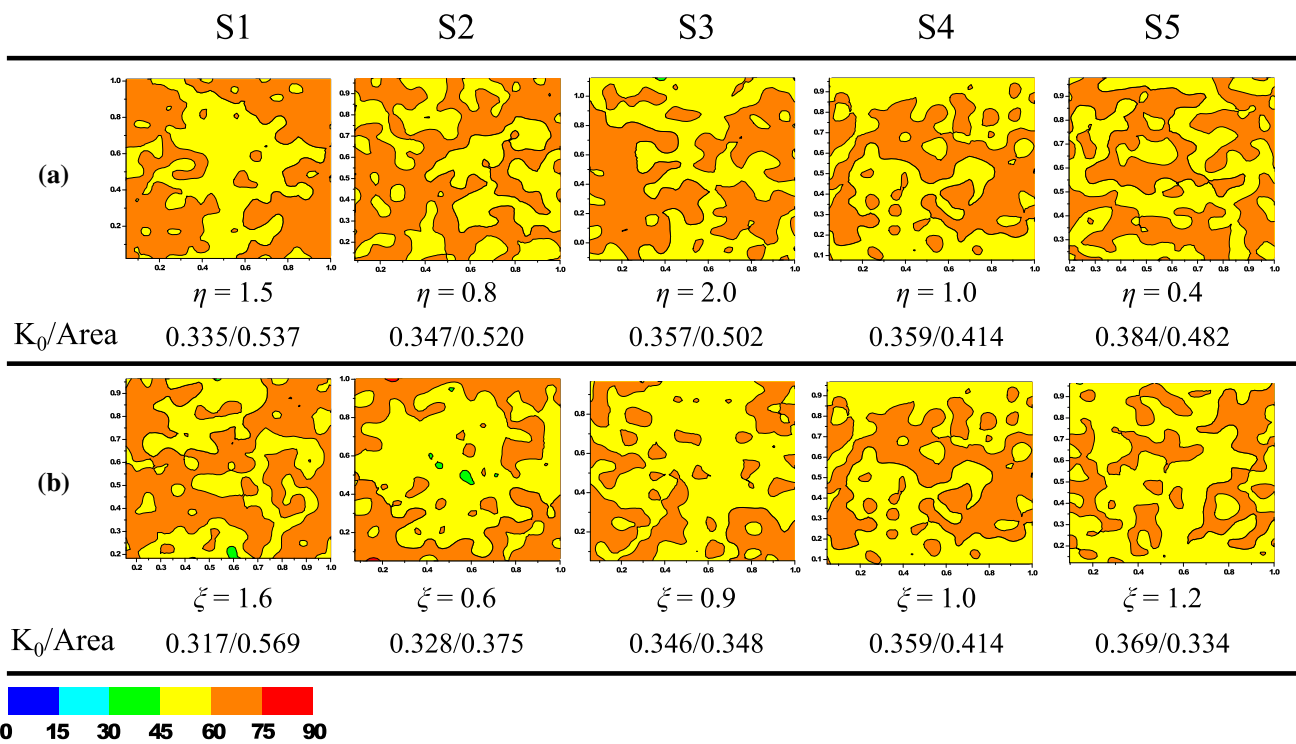


Fig. 15 Contour at final state of θ_k for **a** ellipsoids; **b** superballs

5. Analytical relationship between K_0 and fabric of granular material established in this paper is verified by DEM results, indicating the most crucial role that partition of normal contact force plays in K_0 . From the microscopic perspective, the proportion of contact force partitions of K_0 can be affected by aspect ratio but not blockiness. Moreover, shape-related K_0 partitions can be determined by aspect ratio and blockiness inversely.

Appendix A: Tensors of stress-force-fabric relationship

By analogy to formula of stress tensor [15, 19], integral form of Eq. (4) can be determined as:

$$\sigma_{ij} = \frac{N_c}{V} \int_n E(\mathbf{n}) \bar{f}_i(\mathbf{n}) \bar{d}_j(\mathbf{n}) d\mathbf{n} \tag{A.1}$$

where N_c is the total contact number, $E(\mathbf{n})$ is the probability distribution function (PDF) of contact normal, $\bar{f}_i(\mathbf{n})$ and $\bar{d}_j(\mathbf{n})$ are directional distribution function of contact force vector and branch vector.

The second-order approximation of $E(\mathbf{n})$ takes the expansion form [13]:

$$E(\mathbf{n}) = \frac{1}{4\pi} [1 + G_{ij}^u n_i n_j] \tag{A.2}$$

Second-order tensor G_{ij}^u is determined as:

$$G_{ij}^u = \frac{15}{2} \Phi'_{ij} \tag{A.3}$$

where Φ'_{ij} is the deviatoric part of Φ_{ij} and can be found as $\Phi_{ij} - \delta_{ij} \Phi_{kk} / 3$ (in which δ_{ij} is the Kronecker delta).

$$\Phi_{ij} = \frac{1}{N_c} \sum_{c \in V} n_i n_j \tag{A.4}$$

The second-order approximation of $\bar{f}_n(\mathbf{n})$ or $\bar{d}_n(\mathbf{n})$ can be rewritten as:

$$\bar{f}_n(\mathbf{n}) = \bar{f}_0 [1 + G_{ij}^f n_i n_j] \mathbf{n} \tag{A.5a}$$

$$\bar{d}_n(\mathbf{n}) = \bar{d}_0 [1 + G_{ij}^d n_i n_j] \mathbf{n} \tag{A.5b}$$

And second-order approximation of $\bar{f}_i^i(\mathbf{n})$ or $\bar{d}_j^j(\mathbf{n})$ are:

$$\bar{f}_{i,i}(\mathbf{n}) = \bar{f}_0 [G_{ik}^f n_k - (G_{ki}^f n_k n_i) n_i] \tag{A.6a}$$

$$\bar{d}_{i,j}(\mathbf{n}) = \bar{d}_0 [G_{jk}^d n_k - (G_{ki}^d n_k n_i) n_j] \tag{A.6b}$$

Anisotropic fabric tensors of normal and tangential contact force (G_{ij}^f and G_{ij}^t) or branch vectors (G_{ij}^d and G_{ij}^t) are determined by:

$$K_{ij}^{f_n} = \frac{15 K_{ij}^{f_n}}{2 f_0} \quad G_{ij}^{f_i} = \frac{15 K_{ij}^{f_i}}{3 f_0} \quad \bar{f}_0 = K_{ii}^{f_n} \quad (A.7a)$$

$$K_{ij}^{d_n} = \frac{15 K_{ij}^{d_n}}{2 \bar{d}_0} \quad G_{ij}^{d_i} = \frac{15 K_{ij}^{d_i}}{3 \bar{d}_0} \quad \bar{d}_0 = K_{ii}^{d_n} \quad (A.7b)$$

Corresponding tensor K_{ij}^* (superscript * stands for f_n or d_n) are given by:

$$K_{ij}^{f_n} = \frac{1}{N_c} \sum_{c \in V} \frac{\bar{f}_{n,i} n_j}{1 + G_{kl}^u n_k n_l} \quad (A.8a)$$

$$K_{ij}^{f_i} = \frac{1}{N_c} \sum_{c \in V} \frac{\bar{f}_{t,i} n_j}{1 + G_{kl}^u n_k n_l} \quad (A.8b)$$

$$K_{ij}^{d_n} = \frac{1}{N_c} \sum_{c \in V} \frac{\bar{d}_{n,i} n_j}{1 + G_{kl}^u n_k n_l} \quad (A.8c)$$

$$K_{ij}^{d_i} = \frac{1}{N_c} \sum_{c \in V} \frac{\bar{d}_{t,i} n_j}{1 + G_{kl}^u n_k n_l} \quad (A.8d)$$

Substitutes Eq. (A.2), Eq. (A.5) and Eq. (A.6) into Eq. (A.1) leads to:

$$\begin{aligned} \sigma_{ij} &= \frac{N_c \bar{f}_0 \bar{d}_0}{4\pi V} \int_n (1 + G_{ij}^u n_i n_j) \\ &\times (n_i + G_{ik}^f n_k + (G_{kl}^{f_n} - G_{kl}^{f_i}) n_k n_i n_j) \\ &\times (n_j + G_{jk}^d n_k + (G_{kl}^{d_n} - G_{kl}^{d_i}) n_k n_i n_j) d(\mathbf{n}) \end{aligned} \quad (A.9)$$

We decompose stress tensor as a sum of isotropic term and anisotropic term, Eq. (A.9) is rewritten as:

$$\sigma_{ij} = \frac{N_c \bar{f}_0 \bar{d}_0}{4\pi V} \int_n (E_{ij}^I + E_{ij}^A) (f_i^I + f_i^A) (d_j^I + d_j^A) d(\mathbf{n}) \quad (A.10)$$

Isotropic and anisotropic terms are given:

$$E_{ij}^I = 1 \quad E_{ij}^A = G_{ij}^u n_i n_j \quad (A.11a)$$

$$f_i^I = n_i \quad f_i^A = G_{ik}^f n_k + (G_{kl}^{f_n} - G_{kl}^{f_i}) n_k n_i n_j \quad (A.11b)$$

$$d_j^I = n_j \quad d_j^A = G_{jk}^d n_k + (G_{kl}^{d_n} - G_{kl}^{d_i}) n_k n_i n_j \quad (A.11c)$$

Appendix B: Decomposition of stress tensor

Finally, partitions of stress tensor can be determined as:

$$\sigma_{ij} = C(\sigma_{ij}^0 + \sigma_{ij}^u + \sigma_{ij}^f + \sigma_{ij}^d + \sigma_{ij}^{ud} + \sigma_{ij}^{uf} + \sigma_{ij}^{df} + \sigma_{ij}^{udf}) \quad (B.1)$$

where

$$C = \frac{N_c \bar{f}_0 \bar{d}_0}{4\pi V} \quad (B.2a)$$

$$\sigma_{ij}^0 = \int_n n_i n_j d\mathbf{n} \quad (B.2b)$$

$$\sigma_{ij}^u = \int_n E_{ij}^A n_i n_j d\mathbf{n} \quad (B.2c)$$

$$\sigma_{ij}^f = \int_n f_i^A n_j d\mathbf{n} \quad (B.2d)$$

$$\sigma_{ij}^d = \int_n n_i d_j^A d\mathbf{n} \quad (B.2e)$$

$$\sigma_{ij}^{ud} = \int_n E_{ij}^A n_i d_j^A d\mathbf{n} \quad (B.2f)$$

$$\sigma_{ij}^{uf} = \int_n E_{ij}^A f_i^A n_j d\mathbf{n} \quad (B.2g)$$

$$\sigma_{ij}^{df} = \int_n f_i^A d_j^A d\mathbf{n} \quad (B.2h)$$

$$\sigma_{ij}^{udf} = \int_n E_{ij}^A f_i^A d_j^A d\mathbf{n} \quad (B.2i)$$

Substitutes Eq. (A.11), Eq. (B.2) into Eq. (B.1) we link up the σ_{ij} and $G_{ij}^{(*)}$ tensors (superscript * stands for u, f_n, f_i, d_n and d_i).

Isotropic and anisotropic terms are individual now, and stress tensors is derived by these two terms (third-order terms are neglected):

$$\sigma_{ij}^0 = C \delta_{ij} \quad (B.3a)$$

$$\sigma_{ij}^u = C \frac{2}{5} G_{ij}^u \quad (B.3b)$$

$$\sigma_{ij}^f = C \left(\frac{2}{5} G_{ij}^{f_n} + \frac{3}{5} G_{ij}^{f_i} \right) \quad (B.3c)$$

$$\sigma_{ij}^d = C \left(\frac{2}{5} G_{ij}^{d_n} + \frac{3}{5} G_{ij}^{d_i} \right) \quad (B.3d)$$

$$\begin{aligned} \sigma_{ij}^{ud} &= C \left(\frac{2}{5} G_{ik}^u G_{jk}^{d_i} + \frac{4}{35} G_{ik}^u G_{jk}^D \right. \\ &\quad \left. + \frac{4}{35} G_{ik}^D G_{jk}^u + \frac{2}{35} G_{kl}^u G_{kl}^D \delta_{ij} \right) \end{aligned} \quad (B.3e)$$

$$G_{ij}^D = G_{ij}^{d_n} - G_{ij}^{d_i} \quad (B.3f)$$

$$\begin{aligned} \sigma_{ij}^{uf} &= C \left(\frac{2}{5} G_{ik}^u G_{jk}^{f_i} + \frac{4}{35} G_{ik}^u G_{jk}^F \right. \\ &\quad \left. + \frac{4}{35} G_{ik}^F G_{jk}^u + \frac{2}{35} G_{kl}^u G_{kl}^F \delta_{ij} \right) \end{aligned} \quad (B.3g)$$

$$G_{ij}^F = G_{ij}^{f_n} - G_{ij}^{f_i} \quad (B.3h)$$

$$\begin{aligned} \sigma_{ij}^{df} &= C \left(G_{jk}^{d_i} G_{ik}^{f_i} + \frac{2}{5} G_{jk}^D G_{ik}^{f_i} + \frac{2}{5} G_{jk}^{d_i} G_{ik}^F \right. \\ &\quad \left. + \frac{4}{35} G_{ik}^D G_{jk}^F + \frac{4}{35} G_{ik}^F G_{jk}^D + \frac{2}{35} G_{kl}^D G_{kl}^F \delta_{ij} \right) \end{aligned} \quad (B.3i)$$

Acknowledgements This work was financially supported by the National Natural Science Foundation of China (by Project No. 51909095, No. 51679207 and No. 11972030), Guangdong Basic and Applied Basic Research Foundation (2020A1515011525), and the Fundamental Research Funds for Central Universities (D2192710). Any opinions, findings, and conclusions or recommendations expressed in this material are those of the authors and do not necessarily reflect the views of the financial bodies.

References

- Barr AH (1981) Superquadrics and angle-preserving transformations. *IEEE Comput Graphics Appl* 1(1):11–23
- Christoffersen J, Mehrabadi MM, Nemat-Nasser S (1981) A micromechanical description of granular material behavior. *J Appl Mech* 48(2):339–344
- Chu J, Gan C (2004) Effect of void ratio on k_0 of loose sand. *Géotechnique* 54(4):285–288
- Cleary PW, Hilton JE, Sinnott MD (2017) Modelling of industrial particle and multiphase flows. *Powder Technol* 314:232–252
- de Bono JP, McDowell GR (2016) Investigating the effects of particle shape on normal compression and overconsolidation using DEM. *Granul Matter* 18(3):1–10
- Gao Y, Wang Y (2014) Experimental and dem examinations of k_0 in sand under different loading conditions. *J Geotech Geoenviron Eng* 140(5):04014012
- Gu X, Hu J, Huang M (2015) k_0 of granular soils: a particulate approach. *Granul Matter* 17(6):703–715
- Gu X, Hu J, Huang M, Yang J (2018) Discrete element analysis of the k_0 of granular soil and its relation to small strain shear stiffness. *Int J Geomech* 18(3):06018003
- Guo P (2010) Effect of density and compressibility on k_0 of cohesionless soils. *Acta Geotech* 5(4):225–238
- Guo P, Stolle D (2006) Fabric and particle shape influence on k_0 of granular materials. *Soils Found* 46(5):639–652
- Guo N, Zhao J (2013) The signature of shear-induced anisotropy in granular media. *Comput Geotech* 47:1–15
- Jaky J (1944) The coefficient of earth pressure at rest. *J Soc Hung Archit Eng* 25:355–358
- Kanatani K-I (1984) Stereological determination of structural anisotropy. *Int J Eng Sci* 22(5):531–546
- Lee J, Yun TS, Lee D, Lee J (2013) Assessment of k_0 correlation to strength for granular materials. *Soils Found* 53(4):584–595
- Li X, Yu H (2011) Tensorial characterisation of directional data in micromechanics. *Int J Solids Struct* 48(14–15):2167–2176
- Lirer S, Flora A, Nicotera M (2011) Some remarks on the coefficient of earth pressure at rest in compacted sandy gravel. *Acta Geotech* 6(1):1–12
- Lopera Perez J, Kwok C, O’Sullivan C, Huang X, Hanley K (2015) Numerical study of one-dimensional compression in granular materials. *Géotech Lett* 5(3):96–103
- Northcutt S, Wijewickreme D (2013) Effect of particle fabric on the coefficient of lateral earth pressure observed during one-dimensional compression of sand. *Can Geotech J* 50(5):457–466
- Ouadfel H, Rothenburg L (2001) Stress-force-fabric relationship for assemblies of ellipsoids. *Mech Mater* 33(4):201–221
- Perez JL, Kwok C, Huang X, Hanley K et al (2016) Assessing the quasi-static conditions for shearing in granular media within the critical state soil mechanics framework. *Soils Found* 56(1):152–159
- Radjai F, Wolf DE, Jean M, Moreau J-J (1998) Bimodal character of stress transmission in granular packings. *Phys Rev Lett* 80(1):61
- Sadrekarimi A, Olson SM (2011) Critical state friction angle of sands. *Géotechnique* 61(9):771–783
- Santana T, Candeias M (2018) Effect of void ratio on k_0 of a sand by means of triaxial stress-path testing. *Geotech Geol Eng* 36(1):257–266
- Sarma S, Tan D (2006) Determination of critical slip surface in slope analysis. *Géotechnique* 56(8):539–550
- Tian Q-H, Xu Z-W, Zhou G-Q, Zhao X-D, Kun H (2009) Coefficients of earth pressure at rest in thick and deep soils. *Min Sci Technol* 19(2):252–255
- Wanatowski D, Chu J, Gan C (2009) Compressibility of Changi sand in k_0 consolidation. *Geomech Eng* 1(3):241–257
- Wang Y-H, Gao Y (2014) Examining the behavior and mechanisms of structuration in sand under the k_0 condition. *Granul Matter* 16(1):55–68
- Weng M-C, Cheng C-C, Chiou J-S (2014) Exploring the evolution of lateral earth pressure using the distinct element method. *J Mech* 30(1):77–86
- Williams JR, Pentland AP (1992) Superquadrics and modal dynamics for discrete elements in interactive design. *Eng Comput* 9(2):115–127
- Yan W, Dong J (2011) Effect of particle grading on the response of an idealized granular assemblage. *Int J Geomech* 11(4):276–285
- Yang J, Dai B (2011) Is the quasi-steady state a real behaviour? A micromechanical perspective. *Géotechnique* 61(2):175–183
- Yun TS, Lee J, Lee J, Choo J (2015) Numerical investigation of the at-rest earth pressure coefficient of granular materials. *Granul Matter* 17(4):413–418
- Zhang T, Zhang C, Yang Q, Fu R (2020) Inter-particle friction and particle sphericity effects on isotropic compression behavior in real-shaped sand assemblies. *Comput Geotech* 126:103741
- Zhao S, Zhao J (2019) A poly-superellipsoid-based approach on particle morphology for dem modeling of granular media. *Int J Numer Anal Meth Geomech* 43(13):2147–2169
- Zhao S, Zhao J (2021) SudoDEM: unleashing the predictive power of discrete element method on simulation of non-spherical granular particles. *Comput Phys Commun* 259:107670
- Zhao S, Zhou X (2017) Effects of particle asphericity on the macro-and micro-mechanical behaviors of granular assemblies. *Granul Matter* 19(2):38
- Zhao S, Zhang N, Zhou X, Zhang L (2017) Particle shape effects on fabric of granular random packing. *Powder Technol* 310:175–186
- Zhao S, Evans TM, Zhou X (2018) Shear-induced anisotropy of granular materials with rolling resistance and particle shape effects. *Int J Solids Struct* 150:268–281
- Zhao S, Evans T, Zhou X (2018) Effects of curvature-related dem contact model on the macro-and micro-mechanical behaviours of granular soils. *Géotechnique* 68(12):1085–1098
- Zhao Y, Yang H, Huang L, Chen R, Chen X, Liu S (2019) Mechanical behavior of intact completely decomposed granite soils along multi-stage loading-unloading path. *Eng Geol* 260:105242
- Zhao Y, Yang H, Chen Z, Chen X, Huang L, Liu S (2019) Effects of jointed rock mass and mixed ground conditions on the cutting efficiency and cutter wear of tunnel boring machine. *Rock Mech Rock Eng* 52(5):1303–1313
- Zhu J-G, Jiang M-J, Lu Y-Y, Guo W-L, Zhang B (2018) Experimental study on the k_0 coefficient of sandy gravel under different loading conditions. *Granul Matter* 20(3):40

Publisher's Note Springer Nature remains neutral with regard to jurisdictional claims in published maps and institutional affiliations.